

**Imperial College
London**

Department of Physics

MSci Project Report

Percolation processes during the Epoch of Reionization and preceding cosmic phases

by

00935664

Supervised by
DR. JONATHAN PRITCHARD

Assessed by
PROF. ALAN HEAVENS

Project code: ASTR-Pritchard-1

Word count: approx. 10,000

August 27, 2018

Abstract

Reionization of hydrogen in the intergalactic medium at high redshifts is analyzed as a formal percolation process. We discuss the evolution of the order parameter for this phase transition and relate it to Minkowski functionals. The size distribution of ionized regions is calculated with two complementary techniques: the number density of clusters and granulometry. We extend our analysis to the heating and cooling eras which lead to reionization. The results show consistent behaviour throughout these different processes: a percolating cluster appears at a low filling fraction and the ionized or neutral, hot or cold medium forms a single interconnected region. Zero points in the Euler characteristic, as well as extrema in integral mean curvature, are found to be closely related to the onset of percolation transitions.

Acknowledgements

Firstly, I would like to thank my father and mother, who gifted me with the education that culminated with this project.

I thank my project partner for all the fruitful discussions throughout the past eight months—not to mention the constant support after many hours spent debugging code together and trying to interpret complicated graphs.

Last but not least, I thank our supervisor Dr. Pritchard for his time and patience during our weekly meetings. I have learned a lot from him and am very grateful for his guidance.

Nomenclature

Cosmology symbols

H I	Neutral hydrogen
H II	Ionized hydrogen
z	Cosmological redshift
$x_{\text{H}_\text{I}}(\mathbf{r}, t)$	Fraction of neutral hydrogen at (\mathbf{r}, t)
x_i	Global fraction of ionized hydrogen
$x_{i,c}$	Critical ionized fraction
$x_{\text{th},i}$	Threshold in the degree of ionization of cells

Abbreviations

OP	Order parameter
MF	Minkowski functional
GRF	Gaussian random field
EoR	Epoch of Reionization
IGM	Intergalactic medium
CMB	Cosmic Microwave Background

Contents

1	Introduction	1
1.1	The first billion years	1
1.2	Goals and relation to previous work	3
2	Fundamentals of the 21 cm line	4
3	Measures of morphology, topology and order	9
3.1	Percolation theory	9
3.1.1	Definitions	9
3.1.2	Cluster labelling	10
3.1.3	Results from random site percolation	11
3.2	Minkowski functionals	13
3.2.1	Definitions	14
3.2.2	Properties and examples	14
3.3	Granulometry	15
3.3.1	Description of the method	16
3.3.2	Test on disks with Gaussian-distributed sizes	17
4	Gaussian Random Fields	19
4.1	Mathematical formulation	19
4.2	Results and discussion	21
4.2.1	Order parameter and cluster number density	21
4.2.2	Minkowski functionals	24
4.2.3	Granulometry	26
5	Reionization, heating and cooling	28
5.1	Reionization	29
5.1.1	Order parameter for reionization and its reverse process	29
5.1.2	Size distributions in the ionization field	33
5.1.3	Minkowski functionals and their relation to percolation	35
5.2	Heating and cooling	40
5.2.1	Order parameters for hot and cold gas	40
5.2.2	Minkowski functionals	43
6	Conclusion	50
References		52

CHAPTER 1

Introduction

1.1 The first billion years

According to standard cosmology¹, about 13.8 billion years ago the Big Bang gave birth to a hot soup of fundamental particles in an expanding Universe. In the first few minutes of its infancy, the Universe coalesced into a plasma of atomic nuclei (mostly of hydrogen and helium), electrons and photons, too hot to combine and form neutral atoms. With all its matter fully ionized, the Universe was kept in thermal equilibrium by the efficient Thompson scattering of photons and free electrons until it cooled enough to allow the formation of neutral hydrogen (H I), the event referred to as *recombination*. This occurred around $t \approx 400,000$ years ($z \approx 1100$) and quickly turned the entire Universe neutral. Only a very small residual of ionized hydrogen (H II) remained, a fraction of order $x_i \sim 10^{-3}\text{--}10^{-5}$ of the total number of baryons. Recombination led to the decoupling of photons from matter; light began to propagate freely through the Universe, creating a glow from the primordial plasma which we now see as Cosmic Microwave Background (CMB) radiation. The CMB provides a snapshot of the Universe at this very early stage and our understanding of structure is based on the tiny anisotropies in its temperature (~ 1 part in 100,000).

Fast-forward one billion years and the Universe is rich in texture: galaxies, and larger-scale structures permeate the intergalactic medium (IGM). The oldest galaxies observed to date are from this period (e.g. [Oesch et al., 2016](#); [Zitrin et al., 2015](#)). So the question remains: how did the complexity that surrounds us today arise from the smooth Universe we observe appearing from the Big Bang?

We also observe that the IGM is once again entirely ionized. The Gunn–Peterson test ([Gunn & Peterson, 1965](#)) has allowed us to deduce from hydrogen Ly α observations that the neutral fraction must be very low by $z \gtrsim 6$ ($t \sim 1$

¹The texts by [Loeb and Furlanetto \(2013\)](#) and [Mo, van den Bosch, and White \(2010\)](#), and the reviews by [Pritchard and Loeb \(2012\)](#) and [Furlanetto, Oh, and Briggs \(2006\)](#) serve as primary references for this section, among others.

billion years). Therefore, the Universe must have experienced a phase transition, in going from neutral back to ionized, during the first billion years. This process is known as *reionization* and much effort has been devoted in recent years in trying to understand how it happened.

Theory predicts that for the first 150 million years following recombination, the Universe lingered in a cosmic “Dark Age”, a cold era when no luminous objects yet existed. During this time, gravitational collapse gradually caused small-scale structures to form. The first stars were born, followed by the earliest galaxies, and the Universe began to heat. Eventually, these first sources of radiation became energetic enough to emit UV photons and ionize hydrogen. Reionization is expected to have begun around the most energetic sources in bubbles of H II ([Pritchard & Loeb, 2012](#)). Ionizing photons travelled freely through these bubbles until they reached the neutral IGM, where they were quickly absorbed, due to a very low mean free path in H I. As ionized bubbles grew and more were created, they began to overlap and organize into more complex formations. Soon, reionization was complete. This was the last global phase transition in the history of the Universe. It was also the time when all baryons became directly affected by structure formation—although only a small fraction of these reside in galaxies—and the fuel supply for the birth of all future galaxies (i.e. the IGM) was altered ([Furlanetto et al., 2006](#)).

The general picture described above for this intermediary period (between recombination and our deepest galaxy surveys) is well established, however it is largely untested and continues to be a mystery; it is the next frontier in observational cosmology. In the search for answers, two principal paths are being attempted. The first is to continue to develop current methods and build bigger, more powerful telescopes (e.g. the Giant Magellan Telescope (GMT) ([GMT Observatory, 2012](#)), the Atacama Large Millimeter/submillimeter Array (ALMA) ([ALMA, n.d.](#)), and the James Webb Space Telescope (JWST) ([STScI, 2012](#))). The second is to measure radio emissions and absorptions of hydrogen atoms corresponding to redshifted 21 cm photons. These are produced by the hyperfine transition in ground state H I. Its spectral line is hence a characteristic indicator of the presence of neutral hydrogen. (Ionized hydrogen, with no hyperfine structure, does not interact with this radiation.)

Variations in the 21 cm signal can be used to create 3d maps of the distribution of H I in the IGM throughout most of our horizon volume, and in particular during reionization and the Dark Ages. Thus, 21 cm imaging provides an important tool to complement source observations (of galaxies, etc.). Several large radio interferometer arrays have been built for this purpose (e.g. the LOw Frequency ARray (LOFAR) ([LOFAR, n.d.](#)), the Precision Array to Probe the Epoch of Reionization (PAPER) ([Bradley, 2017](#)) and the Giant Metrewave Radio Telescope (GMRT) ([NCRA, n.d.](#))); with the next generation of instruments, such as the Square Kilometre Array (SKA) ([SKA Org., 2015](#)) and its precursor, the Hydrogen Epoch of Reionization Array (HERA) ([DeBoer et al., 2017](#)), planning to probe even deeper into the Cosmic Dawn, although there

are still many technical challenges to overcome before detailed maps of 21 cm fluctuations are obtained (e.g. [Mellema et al., 2013](#)). The first observation of the mean (sky-averaged) 21 cm signal at redshifts $z \gtrsim 14$ has just recently been accomplished by EDGES (the Experiment to Detect the Global Epoch of Reionization Signature) ([Bowman, Rogers, Monsalve, Mozdzen, & Mahesh, 2018](#)) and has made the first step in opening this treasure trove of information. Our project is motivated by the prospects of this second approach.

1.2 Goals and relation to previous work

Building on the work of [Furlanetto and Oh \(2016\)](#), we examine reionization formally as a percolation process, in which the concept of ionized bubbles growing in isolation is relevant only up to a critical global ionized fraction. Beyond this point, the Universe is dominated by a single percolating cluster and our interpretation of the geometry of reionization must change. Using the same simulation tool called 21cmFAST ([Mesinger, Furlanetto, & Cen, 2011](#)) to generate data from the Epoch of Reionization (EoR), we attempt to reproduce their key results and relate them to other morphological and topological measures that have been employed in the field. In particular, we search for connections to Minkowski functionals (MFs), which have been studied extensively in the literature (e.g. [Friedrich, Mellema, Alvarez, Shapiro, & Iliev, 2011](#); [Yoshiura, Shimabukuro, Takahashi, & Matsubara, 2017](#)). Also, we apply the granulometric characterization of bubble sizes, introduced recently by [Kakiichi et al. \(2017\)](#), to complement the volume statistics obtained with percolation theory (known in the literature as using the ‘Friends-of-Friends’ method). We extend our analysis of 21 cm fluctuations to the heating and cooling stages of the Universe, which lead to reionization. A better understanding of both the local geometry, such as the shapes and sizes of ionized regions, and global geometry, e.g. the Minkowski functionals, of this era will help place constraints on the properties of the first stars and galaxies. Parameters such as the luminosity of ionizing sources, their population, ionizing efficiency, and whether or not they are suppressed in H II, are all integral to the morphology and topology of the Epoch of Reionization ([Friedrich et al., 2011](#)).

This report is structured as follows. In Chapter 2, the physics underlying the 21 cm signal is summarized. In Chapter 3, percolation theory, Minkowski functionals and granulometry are introduced in turn and the background on these methods is given. In Chapter 4, we apply our analysis to Gaussian random fields (GRFs) and discuss the effects of correlations in a random field on the outcomes of these measures. In Chapter 5, we present and discuss our results for reionization and the preceding cosmic phases. Finally, we summarize the conclusions of our project in Chapter 6 and hint at subjects for future research.

CHAPTER 2

Fundamentals of the 21 cm line

The ground state of atomic hydrogen is composed of three symmetric spin states (triplet, spin 1; referred to collectively as *state 2*) and one antisymmetric spin state (singlet, spin 0; referred to as *state 1*). The hyperfine interaction splits the energy levels of these states, causing the triplet states to sit $\Delta E = 5.87 \mu\text{eV}$ above the singlet state. This corresponds to a frequency $\nu_0 = 1.42 \text{ GHz}$ or a wavelength of 21.1 cm (giving the corresponding spectral line its name) and to a temperature $T_* = 68 \text{ mK}$. The 21 cm transition is in fact highly forbidden, with an Einstein coefficient for spontaneous emission $A_{21} = 2.85 \cdot 10^{-15} \text{ s}^{-1}$. Nonetheless, it is one of the most important astrophysical probes simply given the immense quantity of hydrogen in the Universe and the efficiency of the pumping mechanisms which feed the triplet state ([Zaroubi, 2013](#)).

In order to understand and analyze 3d maps of the 21 cm signal we must first see how it arises in observations. The intensity of radiation leaving a cloud of gas, located along a given line of sight, directed towards a known background, is calculated by considering the amount being transmitted through the cloud and the amounts being absorbed and emitted within the cloud—a calculation known as radiative transfer. In the case of 21 cm observations, the gas cloud is neutral hydrogen. When studying this signal across the entire sky, the CMB is taken to be the background source. The equation for radiative transfer is usually written in terms of the specific intensity of the radiation, defined as $I_\nu := dI/d\nu$, where I is the intensity and ν is the frequency. Its standard form is given by

$$\frac{dI_\nu}{ds} = -\alpha_\nu I_\nu + j_\nu, \quad (2.1)$$

where s is the proper length along the path of the light ray, and α_ν and j_ν are the absorption and emission coefficients, respectively. ‘Absorption’, in fact, includes stimulated emission. We follow the prescription in the publicly available lecture notes by [Blackman \(n.d.\)](#) to solve this equation.

The optical depth is defined as

$$\tau_\nu(s) := \int_{s_0}^s \alpha_\nu(s') ds', \quad (2.2)$$

and hence we have $d\tau_\nu = \alpha_\nu ds$. This is a measure of the opacity of a medium. Rewriting eq. (2.1) in terms of τ_ν will become convenient. This gives

$$\frac{dI_\nu}{d\tau_\nu} = -I_\nu + S_\nu, \quad (2.3)$$

where we have defined the source function $S_\nu := j_\nu / \alpha_\nu$. This equation is solved by the integrating factor method:

$$\frac{d(I_\nu e^{\tau_\nu})}{d\tau_\nu} = S_\nu e^{\tau_\nu}, \quad (2.4)$$

so the solution is

$$I_\nu e^{\tau_\nu} = I_\nu(\tau_\nu = 0) + \int_0^{\tau_\nu} S_\nu(\tau') e^{\tau'} d\tau', \quad (2.5)$$

where $\tau_\nu = 0$ implies $s = s_0$, as can be seen from the definition in eq. (2.2), and hence $I_\nu(0)$ is the specific intensity of the background, in our case the CMB spectrum.

Assuming a constant source function, we have

$$\begin{aligned} I_\nu &= I_\nu(0)e^{-\tau_\nu} + S_\nu e^{-\tau_\nu} \int_0^{\tau_\nu} e^{\tau'} d\tau' \\ &= I_\nu(0)e^{-\tau_\nu} + S_\nu(1 - e^{-\tau_\nu}). \end{aligned} \quad (2.6)$$

By considering the cloud of hydrogen as a two-level system with states 1 and 2 (the singlet and triplet), the absorption and emission coefficients can be written in terms of the Einstein coefficients and the population of the states, giving a source function (Rybicki, 1979)

$$S_\nu = \frac{2h\nu^2\nu_0}{c^2} \left(\frac{g_2 n_1}{g_1 n_2} - 1 \right)^{-1}, \quad (2.7)$$

where g_i and n_i are, respectively, the statistical weight and the number density of atoms in state i . We differentiate between ν and ν_0 because the absorption coefficient is smeared around ν_0 by a line profile that is not infinitely sharp.

The so-called *spin temperature* T_S (the excitation temperature of the 21 cm transition) is defined through the relation

$$\frac{n_2}{n_1} = \frac{g_2}{g_1} \exp\left(-\frac{T_*}{T_S}\right). \quad (2.8)$$

It is a measure of the relative populations of the ground and excited states of the 21 cm transition. We always have that $T_S \gg T_*$ (Furlanetto, 2016) so this can be expanded to leading order, meaning there are generally three atoms in state 2 for every atom in state 1. Substituting into eq. (2.7), we find

$$\begin{aligned}
S_\nu &= \frac{2h\nu^2\nu_0}{c^2} \left(\exp\left(\frac{T_*}{T_S}\right) - 1 \right)^{-1} \\
&\approx \frac{2h\nu^2\nu_0}{c^2} \frac{T_S}{T_*} \\
&= \frac{2k_B\nu^2}{c^2} T_S,
\end{aligned} \tag{2.9}$$

using the fact that $\hbar\nu_0 = k_B T_*$.

In radio astronomy it is common to express I_ν in terms of the equivalent *brightness temperature* $T_b(\nu)$, defined as the temperature required of a blackbody such that $I_\nu = B_\nu(T_b)$, where $B_\nu(T)$ is the Planck function. Hence, for a blackbody the brightness temperature is equal to the thermodynamic temperature. In the Rayleigh–Jeans limit ($\hbar\nu \ll k_B T$), $B_\nu(T)$ is well approximated by the convenient form:

$$B_\nu(T) \approx \frac{2k_B\nu^2}{c^2} T. \tag{2.10}$$

This is appropriate in the case of 21 cm radiation at the frequencies of interest (Furlanetto, 2016), so we use this simplification. Therefore, we can express the solution in eq. (2.6) in terms of the brightness temperature as

$$T_b = T_{\text{CMB}} e^{-\tau_\nu} + T_S (1 - e^{-\tau_\nu}), \tag{2.11}$$

where we have substituted the form of S_ν in eq. (2.7) and divided by the common factor of $2k_B\nu^2/c^2$.

Observationally, we see the signal as a distortion to the CMB spectrum and hence we quantify it using its *differential brightness temperature*, $\delta T_b := T_b - T_{\text{CMB}}$, given by the expression

$$\delta T_b = (T_S - T_{\text{CMB}})(1 - e^{-\tau_\nu}), \tag{2.12}$$

which is the brightness *emerging* from the cloud. On earth, this creates an *apparent* brightness of

$$\delta T_b^{\text{obs}} = \frac{T_S - T_{\text{CMB}}}{1+z} (1 - e^{-\tau_\nu}). \tag{2.13}$$

Evaluating the optical depth of a cloud of hydrogen gives the final expression the form (Pritchard & Loeb, 2012)

$$\begin{aligned}
\delta T_b^{\text{obs}} &\approx \frac{T_S - T_{\text{CMB}}}{1+z} \tau_\nu \\
&\approx 27x_{\text{H}_1}(1+\delta) \left(1 - \frac{T_{\text{CMB}}}{T_S}\right) \left[\frac{\partial_r v_r}{(1+z) H(z)} \right] \left(\frac{\Omega_b h^2}{0.023} \right) \left(\frac{0.15}{\Omega_m h^2} \frac{1+z}{10} \right)^{1/2} \text{mK},
\end{aligned} \tag{2.14}$$

where x_{H_1} is the fraction of neutral hydrogen, $(1 + \delta_b)$ is the fractional over-density in baryons, and the term in square brackets adjusts for peculiar velocities along the line of sight—these are all space- and time-dependent fields, as is the spin temperature; the last two terms depend on cosmological constants. We have expanded the exponential in eq. (2.13) to first order since $\tau_\nu \ll 1$ at all relevant redshifts (Pritchard & Loeb, 2012).

Putting aside peculiar velocities, this equation shows that the fields of interest are the ionization field, the density field, and the spin temperature. Most notably, we see that only if the spin temperature deviates from T_{CMB} can the signal be detected. The 21 cm signal¹ boils down to the dynamics of these three fields:

$$\delta T_b \sim x_{\text{H}_1} (1 + \delta) \left(1 - \frac{T_{\text{CMB}}}{T_s} \right). \quad (2.15)$$

In this project, we focus on understanding the evolution of the ionization field and the brightness temperature as a whole. An in-depth discussion of the spin temperature and density field is beyond our scope. We note in passing that the main mechanisms which determine T_s and establish the population of the triplet state are (Pritchard & Loeb, 2012): (a) absorption of 21 cm photons from the CMB; (b) collisions with other hydrogen atoms and free electrons; (c) scatterings with Ly α photons which leave the atom in the triplet state after a cascade from higher excited states. The spin temperature is then given by the balance of these effects (Field, 1958):

$$T_s = \frac{T_{\text{CMB}} + y_c T_K + y_\alpha T_\alpha}{1 + y_c + y_\alpha}, \quad (2.16)$$

where T_K is the gas kinetic temperature, T_α is the so-called color temperature of the Ly α radiation field (the temperature obtained by fitting a blackbody shape to the observed flux, which is strongly coupled to T_K), and y_c and y_α are the coupling coefficients for atomic collisions and Ly α scattering, respectively. Detailed considerations of the physics underlying spin temperature fluctuations can be found in the review by Pritchard and Loeb (2012).

Figure 2.1 shows the mean spin temperature, the mean ionized fraction (x_i) and the mean 21 cm brightness predicted by our simulation boxes. Left to its own devices, the CMB would quickly force the hydrogen spin states into thermal equilibrium, setting $T_s = T_{\text{CMB}}$. It is the other two processes which break this trend, as is happening around $z \sim 24$ in our simulation, when the first sources of light turn on. The 21 cm line is then seen in absorption (negative δT_b), since $T_s < T_{\text{CMB}}$. During this regime, the spin temperature is expected to be coupled to cold gas. Around $z \sim 17$, heating of the IGM becomes dominant and the spin temperature is brought back to $T_s = T_K = T_{\text{CMB}}$. Above $z \sim 12$, the 21 cm signal is seen in emission (positive δT_b). Heating continues to drive up T_s as it is still coupled to the gas temperature, until

¹Henceforth, we always refer to the observed differential brightness temperature.

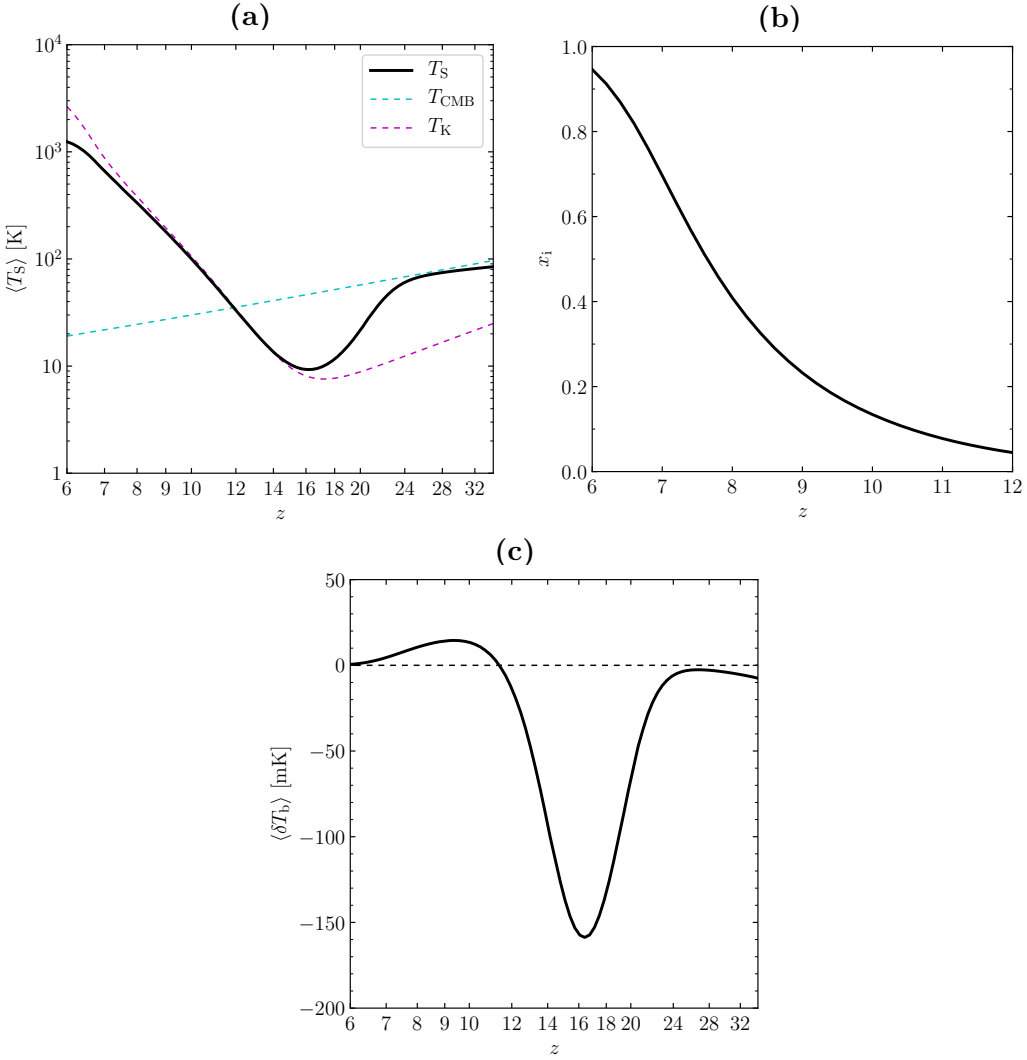


Figure 2.1. (a) the mean spin temperature as a function of redshift for our simulation (shown in black). The CMB temperature and the gas kinetic temperature are shown for reference in cyan and magenta, respectively. (b) the average ionized fraction. (c) the mean differential brightness temperature. The dashed line represents $\delta T_b = 0$. (Cosmic time proceeds from right to left.)

$T_S \sim T_K \gg T_{CMB}$ and the spin temperature factor in eq. (2.15) can be safely ignored (fluctuations tend not to deviate very far from the mean at these low redshifts). The eventual decay of the signal at $z \lesssim 10$ is caused by the reionization of hydrogen. During this period, variations in the ionization field dominate 21 cm fluctuations (Furlanetto, Zaldarriaga, & Hernquist, 2004). In the redshifts $24 \lesssim z \lesssim 34$, the Universe is in the later stages of its Dark Age and no 21 cm signal is detected, although a second absorption trough is expected at higher redshifts (Pritchard & Loeb, 2012).

CHAPTER 3

Measures of morphology, topology and order

In this chapter we introduce the techniques used in our project to analyze 21 cm images and Gaussian random fields. We begin here with the theory and give some simple demonstrations of their use.

3.1 Percolation theory

Percolation theory is a model of phase transitions with a simple mathematical formulation, which nonetheless delivers much insight about the formation of complex structures in random fields. The phenomenon of interest in percolation theory is the growth of clusters and their properties. In understanding reionization as a percolation process, the key statistics we will focus on are the order parameter and the number density of clusters. Percolation theory relies on the capacity to identify clusters with well-defined boundaries. Thus, its most direct application is to binary-valued fields. For continuous fields (e.g. the 21 cm brightness temperature) the problem will arise of how to establish a binarization (discussed in Chapters 4 and 5). For now, we consider a given binary lattice and refer to cells with value 0 as ‘empty’ and cells valued 1 as ‘filled’ or ‘occupied’.

3.1.1 Definitions

A *cluster* is defined as a collection of occupied cells such that there exists a path connecting every pair of cells in the cluster and no member is connected to any additional cells outside the cluster. We consider connections across common faces only—a so-called simple cubic system¹. By *volume* of a cluster

¹This choice is somewhat arbitrary and the general conclusions of percolation theory, such as the appearance and growth of a percolating cluster, do not depend on it. The location of the percolation transition, i.e. the critical fraction (defined below), however, does depend heavily on the lattice structure (Christensen & Moloney, 2005). We will implement

we refer to the number of cells in it.

Formally, *percolation* occurs in an infinite lattice with the appearance of a cluster of infinite volume. In a finite lattice, as in all numerical computations, percolation is said to occur when a single cluster spans (at least) one axis of the lattice. This cluster is then referred to as the *percolating cluster*. Such a structure forms as a fractal, in the sense that its features are scale-invariant.

The volume of the percolating cluster as a fraction of the box volume is the *order parameter* (OP) for percolation, $P_\infty := V_{\text{perc}}/V_{\text{box}}$. Order parameters arise in the study of phase transitions as a measure of the degree of order, where the OP is typically zero in one phase and non-zero in another. We normalize the order parameter by the *filling fraction*, i.e. the total number of filled cells as a fraction of the box volume, $x := V_{\text{filled}}/V_{\text{box}}$, and hereafter refer to

$$\frac{P_\infty}{x} = \frac{V_{\text{perc}}/V_{\text{box}}}{V_{\text{filled}}/V_{\text{box}}} = \frac{V_{\text{perc}}}{V_{\text{filled}}} \quad (3.1)$$

as the OP. Defined this way, the OP describes the probability that a randomly chosen filled (rather than filled *or empty*) cell belongs to the percolating cluster.

The *critical fraction*, x_c , is the value of the filling fraction at which the OP jumps to non-zero values; this marks the beginning of the phase transition. When $P_\infty = x$, all clusters have merged with the percolating cluster and the OP is 1. The end of the transition is at $P_\infty = x = 1$ (in a finite lattice, these might describe different points²).

The number of clusters of volume V , per cell in the box, gives the *number density* of clusters, $dn/dV := (\text{no. clusters of volume } V)/V_{\text{box}}$. We will often plot this as a histogram binned logarithmically, thus shown as $dn/d\ln V = Vdn/dV$.

3.1.2 Cluster labelling

We use the Hoshen–Kopelman algorithm ([Hoshen & Kopelman, 1976](#)) to distinguish and label clusters³. The algorithm scans through a lattice and checks each cell's connections to its neighbour in the previous row, column and stack (3 of 6 total neighbours), i.e. for cell (i, j, k) it checks its connections to cells $\{(i-1, j, k), (i, j-1, k), (i, j, k-1)\}$. An integer label is then assigned to the cell with value depending on whether: (a) the cell is empty (labelled 0); (b) the cell is filled but has no occupied neighbours⁴ (it is a new cluster and given a new label); (c) it is filled and has one or more occupied neighbours with the same label (given that same label); (d) it is filled and connects previously

this choice consistently and discuss all results assuming the same structure.

²In an infinite lattice, there is always a non-zero probability for an occupied cell to be outside the percolating cluster, in whose smallest of gaps it could reside, until all holes are filled and $x = 1$.

³Implementations in Python and C were made available to us by Dr. Pritchard.

⁴To be understood as “no occupied neighbours *in the direction checked*”. These are neighbours that have already been labelled.

separate clusters (given the current label and stores links to previous labels in a list of label equivalencies). The algorithm completes the partitioning with a second pass, where all cells which have equivalent labels are given their lowest identifying label. This is a very fast and efficient way of finding clusters.

3.1.3 Results from random site percolation

To provide a point of reference for subsequent results, we discuss the case of purely random percolation. Here, a $3d$ lattice is initialized with random numbers uniformly distributed between 0 and 1. A filling fraction x is chosen to binarize the lattice, such that cells initialized with values $p \geq x$ are bumped to 1, and cells with $p < x$ are assigned 0. For large enough box sizes (and a good enough random number generator⁵), the probability of a random cell being filled is very close to x . The binarized lattice is then divided into clusters, and these are searched for occupied cells located at opposite faces which belong to the same cluster. The OP is calculated as (no. cells in spanning cluster)/ x , or, if there is no spanning cluster, it is set to 0.

The result obtained for a box with 256^3 cells as a function of filling fraction is shown in Figure 3.1. The abrupt rise in P_∞/x occurs at a critical fraction $x_c = 0.306$, when the percolating cluster is formed; consistent with the literature value, $x_c = 0.3116\dots$ ([Lorenz & Ziff, 1998](#)). Given the finite step size, the actual value lies somewhere between this and the next measured data point ($x = 0.326$). Improvements in accuracy can easily be made by increasing box size and the number of samples in x , but accuracy is not our main objective here and we present this result on the same scale as our fiducial reionization boxes. Beyond the critical fraction, there is a rapid increase in the OP as P_∞ tends to x . By $x \approx 0.4$, the percolating cluster already contains approximately 90% of the occupied cells. The sharp climb is followed by a decelerated approach to 1 (as expected), where, due to the finite nature of the lattice, P_∞/x reaches its maximum before the box is completely filled.

The percolating cluster which exists at $x > x_c$ is unique. This is characteristic of all random percolation models regardless of the details of the model, such as the lattice structure, dimension, or whether it describes bond percolation instead ([Christensen & Moloney, 2005](#)). It is worth noting that these are not good models of reionization, unless it indeed proceeds purely randomly. However, the uniqueness of the percolating cluster applies also to systems which include correlations between cell states ([C. M. Newman & Schulman, 1981](#)). The emergence of the percolating cluster is illustrated in Figure 3.2 (here the lattice is 2-dimensional and contains 512^2 cells).

The cluster labeling of Hoshen and Kopelman provides a simple way of extracting the number density of clusters by counting the occurrences of any given label. The result for the 3-dimensional lattice above, shown in Figure 3.3, is as expected. At the critical point, the distribution follows a power law

⁵We use the basic generators in `numpy.random`.

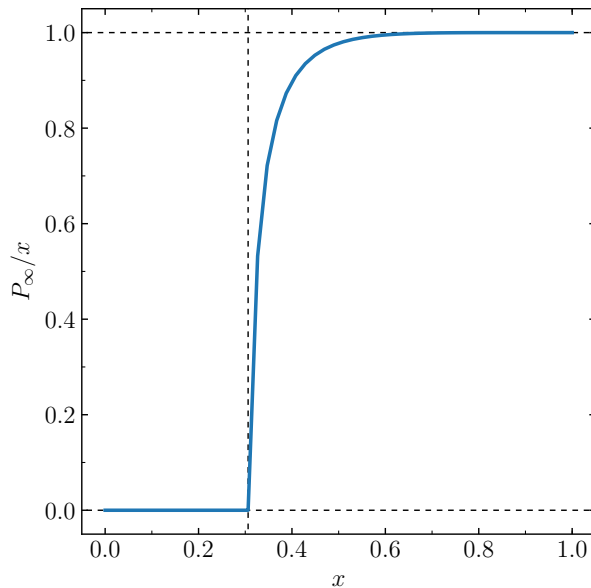


Figure 3.1. Order parameter for random percolation as a function of the filling fraction (or occupation probability). The vertical dashed line shows the critical fraction $x_c = 0.3061$.

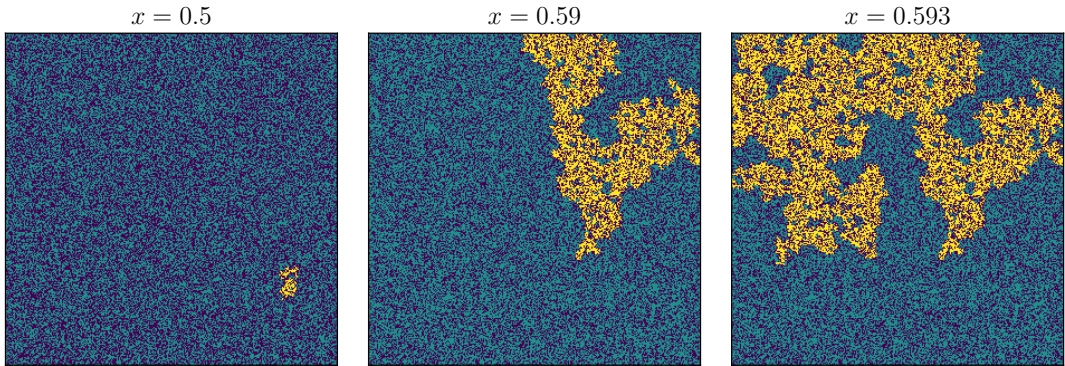


Figure 3.2. Random percolation on a $2d$ lattice of size 512^2 at various occupation probabilities approaching the critical value, $x_c^{d=2} = 0.5927\dots$ ([M. E. J. Newman & Ziff, 2000](#)). Unoccupied cells are shown in purple, the largest cluster is shown in yellow, and all other occupied cells are shown in turquoise. From left to right, the filling fraction is set to $x = 0.5$, $x = 0.59$ and $x = 0.593$ (slightly below, just below and just above the transition, respectively). Notice the critical fraction is higher in $2d$, since a reduced number of nearest neighbours makes it more difficult to form large clusters. The volume of the largest cluster present at each stage is 503, 20934 and 54096 cells. Notice also that much of the percolating cluster is contained within the largest cluster at $x = 0.59$. Only a few more vital connections were necessary for it to percolate by merging with a second very large cluster. This is the nature of the critical filling fraction.

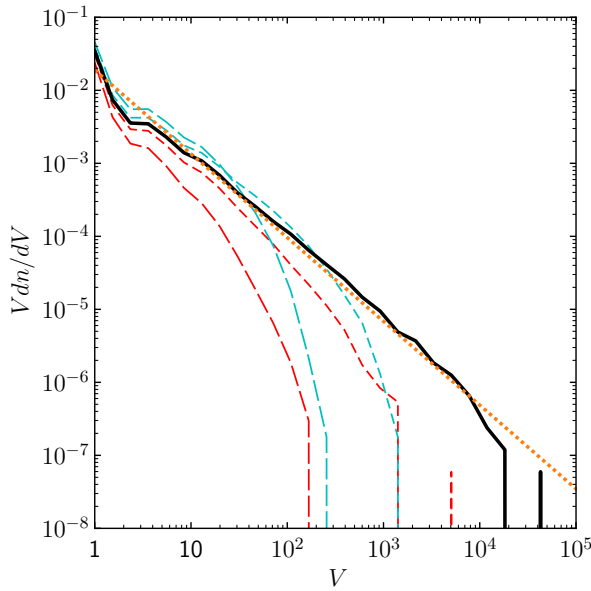


Figure 3.3. Cluster volume distribution at various filling fractions. The black line corresponds to the critical fraction $x_c = 0.306$. The power law scaling $dn/dV \propto V^{-2.15}$ is shown in dotted orange. The dashed curves in red and cyan, respectively, are for the distribution slightly below and above x_c , shown at $x = x_c \pm 0.02$ and $x = x_c \pm 0.06$. The isolated spikes to the bottom-right are a sign of poor statistics at large volumes (bins with a single count) and are due to finite size effects. Those at $V > 10^5$ are truncated from the figure (including the percolating cluster).

very closely, until it cuts off at a high characteristic scale due to the finite size of the lattice. This power law scaling, plotted in dotted orange, goes as $dn/dV \propto V^{-\tau}$ with $\tau = 2.15$, more accurately calculated in the literature as $\tau \approx 2.19$ (Ballesteros et al., 1999). Deviating marginally from this filling fraction, the cutoff scale is remarkably lower, while the distribution at small volumes stays quite close to the power law relation. The cutoff decreases as the distance to the critical fraction, $|x - x_c|$, increases.

3.2 Minkowski functionals

Minkowski functionals are descriptors of spatial patterns which characterize connectivity, shape and content. They are at the heart of integral geometry—an approach to geometry based on integral measures rather than differential quantities. Minkowski functionals have been applied in many areas of physics. For example, to various problems in statistical physics (Mecke, 2000) and to quantify departures from Gaussianity in the CMB (e.g. Schmalzing & Górski, 1998; Eriksen, Novikov, Lilje, Banday, & Górski, 2004). In a similar spirit, they have recently been used in studies of reionization to understand its own non-Gaussianities and to distinguish between different stages of reionization (Gleser, Nusser, Ciardi, & Desjacques, 2006; Lee, Cen, Gott III, & Trac, 2008),

as well as to discriminate between various models of reionization (Friedrich et al., 2011). The topology of the heating era has also begun to be studied using Minkowski functionals (Yoshiura et al., 2017) with an eye for upcoming observations.

We follow Schmalzing and Buchert (1997) in defining the Minkowski functionals and adopt the methods described therein to evaluate them numerically, using code made available to us by Dr. Pritchard.

3.2.1 Definitions

Consider a scalar field $\phi(\mathbf{x})$ on a 3-dimensional space $D \subseteq \mathbb{R}^3$. The *excursion set* of $\phi(\mathbf{x})$ at a given threshold, ϕ_{th} , is defined as the set of points $F_\phi := \{\mathbf{x} \mid \phi(\mathbf{x}) \geq \phi_{\text{th}}\}$, i.e. all points with value greater than (or equal to) the threshold. The four MFs, V_k for $k \in \{0, 1, 2, 3\}$, per unit volume of the total volume $|D|$, on this excursion set are then given by the equations

$$V_0(\phi_{\text{th}}) := \frac{1}{|D|} \int_D \Theta(\phi(\mathbf{x}) - \phi_{\text{th}}) d^3x \quad (3.2)$$

$$V_k(\phi_{\text{th}}) := \frac{1}{|D|} \int_{\partial F_\phi} v_k^{(\text{loc})}(\phi_{\text{th}}, \mathbf{x}) d^2A, \quad (3.3)$$

where Θ is the Heaviside step function⁶. V_k for $k \geq 1$ are integrals over the boundary surface, ∂F_ϕ , of F_ϕ of the local Minkowski functionals:

$$v_1^{(\text{loc})}(\phi_{\text{th}}, \mathbf{x}) := \frac{1}{6} \quad (3.4)$$

$$v_2^{(\text{loc})}(\phi_{\text{th}}, \mathbf{x}) := \frac{1}{6\pi}(\kappa_1 + \kappa_2) \quad (3.5)$$

$$v_3^{(\text{loc})}(\phi_{\text{th}}, \mathbf{x}) := \frac{1}{4\pi}(\kappa_1 \kappa_2), \quad (3.6)$$

where κ_1 and κ_2 are the principal curvatures of ∂F_ϕ at \mathbf{x} . Thus, V_0 is simply the *volume* of F_ϕ and V_1 is its *surface area*. V_2 is the *integral mean curvature* of ∂F_ϕ and V_3 the integral Gaussian curvature, commonly known as the *Euler characteristic*. V_3 is directly related to the (possibly more intuitive) genus number $g = 1 - V_3$ and is proportional to (Friedrich et al., 2011)

$$V_3 \propto (\text{no. parts}) - (\text{no. tunnels}) + (\text{no. cavities}). \quad (3.7)$$

3.2.2 Properties and examples

Minkowski functionals are of special interest because of their *additive* property, and also for their *completeness*. By additive, we mean that the k -th Minkowski

⁶ $\Theta(y) = 1$ for $y \geq 0$, and zero otherwise.

functional, V_k , on the union $A \cup B$ of two domains A and B is the sum $V_k(A) + V_k(B)$ minus the intersection $V_k(A \cap B)$. This makes them robust measures of the global geometry of a system. By completeness, we refer to the theorem by Hadwiger (1957), which states that, under fairly unrestrictive conditions⁷, *any* functional of a d -dimensional domain can be written as a linear combination of the $d+1$ Minkowski functionals (Mecke, 2000).

The normalization given here is that of (Schmalzing & Buchert, 1997), however it is one of many used in the literature (Mecke, 2000), so we discuss relative values. For example, a solid sphere has $\kappa_1 = \kappa_2 = 1/R$, hence $V_3 \cdot |D| = 1$ and $V_2 \cdot |D| = 4R/3$. Alternatively, we could count the sphere as one part with no cavities or tunnels and arrive at the same result. If we had a spherical cavity in an otherwise full box, then $\kappa = -1/R$ and $V_2 \cdot |D| = -4R/3$, but V_3 is the same, since cavities and parts both contribute positively. A spherical shell, on the other hand, has $V_3 \cdot |D| \approx 2$, counts as one part with one cavity, and has $V_2 \approx 0$. For a torus, $V_3 = 0$, since it is composed of one part and one tunnel, while $V_2 < 0$ but depends on the sizes of the inner and outer radii.

Note that under a reflection in orientation of ∂F_ϕ , the principal curvatures transform as $\kappa \rightarrow -\kappa$ at all points, for any $\phi(\mathbf{x})$. Hence, V_2 changes sign while V_3 remains unaffected. This is the case when considering MFs on the complement of F_ϕ , i.e. when thresholding *below* a given value, which becomes relevant when comparing MFs to the order parameter for reionization. We will find that the order parameter does not obey any such simple symmetry and the results for ionized compared to neutral gas—or hot vs. cold gas, before reionization—have to be obtained separately⁸.

3.3 Granulometry

One of the fundamental intricacies of quantifying the morphology of reionization is that there is no single clear-cut definition of the ‘size’ or ‘shape’ of an ionized region. Percolation theory aligns itself naturally to the definition of size as the plain volume of a region. However, there are other meaningful characterizations of size which complement this. For example, in the spherical averaging method (SPA), ‘size’ is defined as the largest radius for which the average ionized fraction in a sphere, around a given cell, is above a certain threshold (e.g. 90%). Zahn et al. (2007) find that the SPA size distribution has a maximum, i.e. a characteristic size, which increases with the global ionization fraction, showing how ionized regions dilate as reionization progresses. Friedrich et al. (2011) calculate a ‘mean size’ using the ratio $3V/A$ of the total volume and surface area of the ionized regions. They find that this also

⁷Specifically, supposing that the functional be additive, motion-invariant and conditionally continuous.

⁸This can be understood with some intuition if one considers the percolation of bubbles vs. percolation of the cavities that overlapping bubbles create. The fundamental shape undergoing percolation, i.e. the percolation model itself, is different.

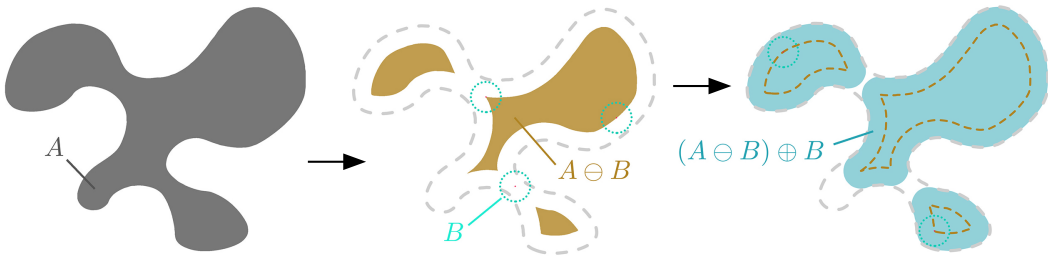


Figure 3.4. The opening of a set A by a structuring element B as the composition of erosion and dilation.

increases with x_i , as expected, although much more gently compared to the SPA peak. They also compute the power spectrum (explained in Chapter 4) for their simulation and identify strong correlations at two scales, 0.8 Mpc and 6 Mpc: a characteristic bubble size and galaxy cluster size, for ionized fractions above $x_i \sim 0.4$. Other interpretations of size have been tested, such as the Watershed method ([Lin, Oh, Furlanetto, & Sutter, 2016](#)) and the mean free path method (e.g. [Giri, Mellema, Dixon, & Iliev, 2018](#)).

The results of these are not to be contrasted as they describe different characterizations of size. Each could, in principle, be used as an independent metric when comparing simulation to observations in order to distinguish between different reionizations. In our project, we investigate the granulometric technique recently put forward by [Kakiichi et al. \(2017\)](#), based on ideas from mathematical morphology. Specifically, the method emerges from the concept of *sieving*, known as morphological *opening*.

3.3.1 Description of the method

Granulometry attempts to recover the underlying size distribution of an object given the shape of its fundamental building block. This building block is referred to as the *structuring element*. We use a sphere as the structuring element, since this seems to be the natural choice for reionization maps, yet it could be useful to learn whether choosing different shapes provides additional insight.

Granulometry regards binary fields as sets. The basic operation we apply is morphological opening, which is a combination of *erosion* and *dilation* of a set. It could be useful to follow along with Figure 3.4 as we define these below. (In practice, they do exactly what the names imply.)

The opening of a set A by a structuring element B is defined as ([Gonzalez & Woods, 2008](#))

$$A \circ B := (A \ominus B) \oplus B \quad (3.8)$$

where \ominus and \oplus are Minkowski subtraction and addition, also known as erosion and dilation.

The erosion of A by B is defined as

$$A \ominus B := \{z \mid (B)_z \subseteq A\}. \quad (3.9)$$

In words, this means $A \ominus B$ is the set of all points z such that B translated by z (i.e. with its center located at z) is contained within A . This generally means trimming the edges of A with an eraser shaped like B .

Dilation is defined by

$$A \oplus B := \{z \mid (\hat{B})_z \cap A \neq \emptyset\}. \quad (3.10)$$

This is the set of all points z such that the reflection of B translated to z —here, reflection can be ignored since we use spheres for B —has a non-empty intersection with A ; which usually means broadening the borders of A with a brush shaped like B .

Combining these into the opening operation also has an intuitive geometrical meaning: we ‘roll’ B along the inside of A and include all the points which are covered by B . The net effect is that opening usually smooths the edges of a shape (erasing thin protrusions) and eliminates narrow bridges between larger components. Note that this is far from a null operation, as one might at first suspect. Features smaller than the structuring element are most affected when opening. Therefore, by progressively opening A with spheres B_R of increasing radius R , we can obtain a cumulative size distribution through the fractional volume removed by each operation ([Kakiichi et al., 2017](#)):

$$F(< R) = 1 - \frac{V[A \circ B_R]}{V[A]}. \quad (3.11)$$

$F(< R)$ is the fraction of structures in A with size smaller than the radius R , since $A \circ B_R$ removes these. From this we can easily get a differential size distribution dF/dR .

3.3.2 Test on disks with Gaussian-distributed sizes

We test the technique in $2d$ for a lattice of size 512^2 , onto which disks of random sizes are sprinkled at random positions. The disk radii are sampled from a Gaussian distribution with mean and standard deviation $(\mu, \sigma) = (15, 3)$, in cell units. We find that the time it takes to do the opening operation takes significantly longer the larger the filled regions⁹. The results are averaged over 30 different runs and normalized such that the total probability is 1. We apply the analysis for filling fractions 0.2 and 0.4, shown in Figure 3.5 with an example realization in each case.

Granulometry recovers the underlying distribution with substantial accuracy, producing slight distortions which tend to cause broadening and a shift to higher radii. The shift is due to the overlapping of disks, since sieves larger than any one bubble can fit inside a cluster of bubbles, causing excess at higher

⁹We use `scipy` to evaluate the opening of a lattice.

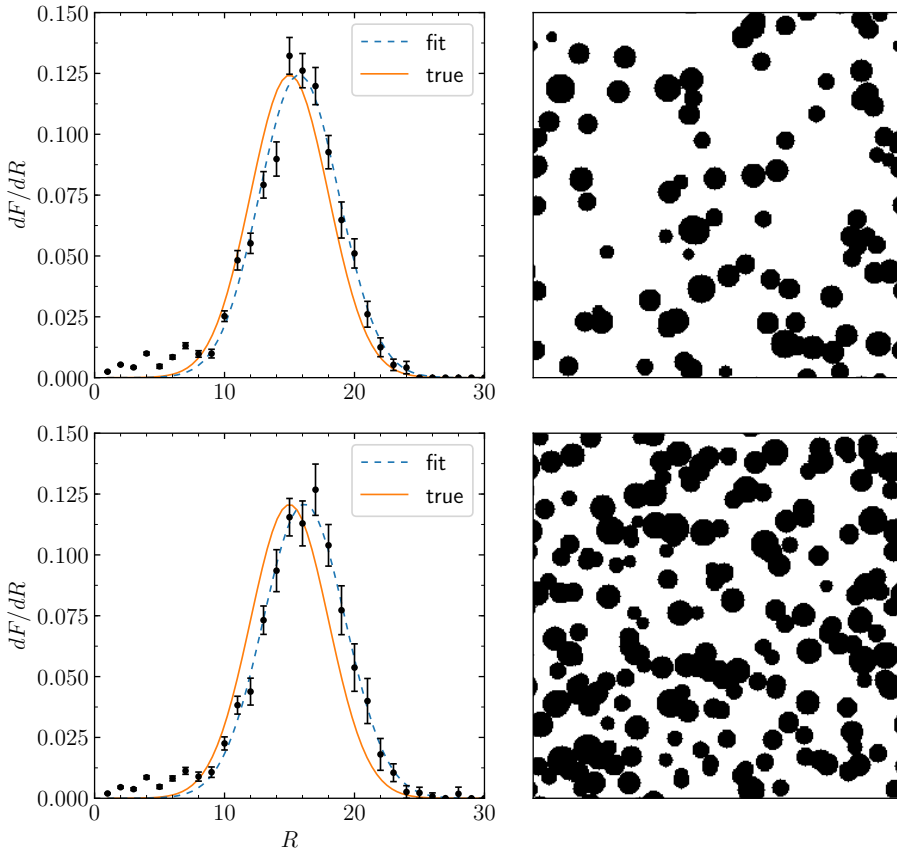


Figure 3.5. Granulometric size distribution for disks of random sizes. Radii are sampled from a Gaussian distribution with $(\mu, \sigma) = (15, 3)$, shown in orange. The blue dashed lines represent the Gaussian curves of best fit. In top row, the disks fill 20% of the image and on the bottom, 40%. The results are averaged over 30 different realizations. Example realizations are shown to the right.

radii and at the cost of counts at lower radii. The output distribution still fits a Gaussian remarkably well for $R \gtrsim 10$. Distortions at very low radii are due to bubbles being cut short around the edges of the lattice and the inability to properly construct disks of radii close to the cell size.

CHAPTER 4

Gaussian Random Fields

In this chapter we present the first part of our results, which apply to Gaussian random fields (GRFs). These fields play a central role in cosmology: the initial density distribution of matter leftover from inflation is believed to be a Gaussian random field, implying that all the complex structure we see today was grown out of small seed fluctuations which followed the quite special statistics of a Gaussian. In the previous chapter we mentioned the relevance of Minkowski functionals to the search for non-Gaussianities in the CMB and 21 cm signal—this precisely means comparing their statistics to those of GRFs. Here, we apply the tools we have described to Gaussian random fields and build a basic intuition for the effects of correlations in a random field. We will show that these have a strong influence on the order parameter—but first, we begin with a brief introduction to the subject.

4.1 Mathematical formulation

A random field¹, $X(\mathbf{t})$, is a function whose values are random variables. If the argument \mathbf{t} is an element of a set containing only a finite number of elements, $\{\mathbf{t}_1, \mathbf{t}_2, \dots, \mathbf{t}_n\}$, then the random vector $\mathbf{X} = (X(\mathbf{t}_1), X(\mathbf{t}_2), \dots, X(\mathbf{t}_n))$ can be considered a single multi-dimensional random variable. For example, the multivariate Gaussian $\mathbf{X} \sim \mathcal{N}_n(\boldsymbol{\mu}, C)$ with mean $\boldsymbol{\mu}$ and covariance matrix C .

Gaussian random fields generalize the concept of a multivariate Gaussian onto continuous spaces, e.g. $\mathbf{t} \in \mathbb{R}^3$ for the usual $3d$ space of interest to us. The *covariance function*, $C(\mathbf{t}, \mathbf{s})$, of a Gaussian random field is the generalization of the covariance matrix (with elements C_{ij}) of a Gaussian random vector, and is expressed analogously as

$$C(\mathbf{t}, \mathbf{s}) = \langle X(\mathbf{t})X(\mathbf{s}) \rangle - \mu(\mathbf{t})\mu(\mathbf{s}), \quad (4.1)$$

where $\mu(\mathbf{t}) := \langle X(\mathbf{t}) \rangle$ is the mean or expectation of X at \mathbf{t} . Just as for

¹Adler and Taylor (2007), Abrahamsen (1997) and Yaglom (1987) are the primary references for this section.

multivariate Gaussians, the statistics of a Gaussian field are fully described by a mean and a covariance function.

The *correlation function*, $\rho(\mathbf{t}, \mathbf{s})$, is defined as

$$\rho(\mathbf{t}, \mathbf{s}) := \frac{C(\mathbf{t}, \mathbf{s})}{\sigma(\mathbf{t})\sigma(\mathbf{s})}, \quad (4.2)$$

where $\sigma^2(\mathbf{t}) := C(\mathbf{t}, \mathbf{t})$ is the variance of X at \mathbf{t} . This is usually the quantity of interest in cosmology.

We are interested in isotropic (rotation-invariant) Gaussian random fields, in which case the covariance function depends only on the distance between two points, i.e. $C(\mathbf{t}, \mathbf{s}) = C(\tau)$ with $\tau := |\mathbf{t} - \mathbf{s}|$. This implies that the field is also stationary (translation-invariant), hence the mean and variance must be constant everywhere, $\sigma(\mathbf{t}) = \sigma$ and $\mu(\mathbf{t}) = \mu$. The correlation and covariance functions then become equivalent:

$$C(\tau) = \sigma^2\rho(\tau). \quad (4.3)$$

We choose $\sigma = 1$ and $\mu = 0$, without any loss of generality in our results, such that $\rho(\tau)$ and $C(\tau)$ become exactly equal and can be expressed simply as

$$\rho(\tau) = C(\tau) = \langle X(\mathbf{t})X(\mathbf{t} + \tau\hat{\mathbf{n}}) \rangle \quad (4.4)$$

for any \mathbf{t} and unit direction $\hat{\mathbf{n}}$. This measures the degree of correlation in the values of the field at any two points separated by a distance τ .

In radio astronomy, it is common to work with the spectral representation of the correlation function, known as the *power spectrum* (or *spectral density*) $P(k)$ and given by the Fourier transform of $\rho(\tau)$,

$$P(k) = FT[\rho(\tau)], \quad (4.5)$$

since interferometers make observations in Fourier coordinates.

We generate isotropic GRFs using the ‘moving average’ method by first sampling an arbitrary isotropic power spectrum of choice², $P(k)$, at all \mathbf{k} with components of magnitude $|k_i| \leq L/2$; these being the (spatial) frequencies which fit into a box of size L . We then obtain the Fourier representation of a Gaussian random field by multiplying $\sqrt{P(k)}$ with Gaussian noise ([Adler & Taylor, 2007](#); [Holmes-Cerfon, 2008](#)). This gives us

$$\hat{X}(\mathbf{k}) = \sqrt{P(k)}(A_{\mathbf{k}} + iB_{\mathbf{k}}), \quad (4.6)$$

where $\hat{X}(\mathbf{k}) = FT[X(\mathbf{t})]$, and $A_{\mathbf{k}}$ and $B_{\mathbf{k}}$ are independent random variables sampled at each point \mathbf{k} from a Gaussian of mean zero and variance one. Evaluating the inverse Fourier transform of the result then gives us two independent realizations of a Gaussian random field, $\text{Re}[X(\mathbf{t})]$ and $\text{Im}[X(\mathbf{t})]$, with mean zero and correlation function $\rho(\tau) = FT^{-1}[P(k)]$.

²The power spectrum must be square-integrable, however.

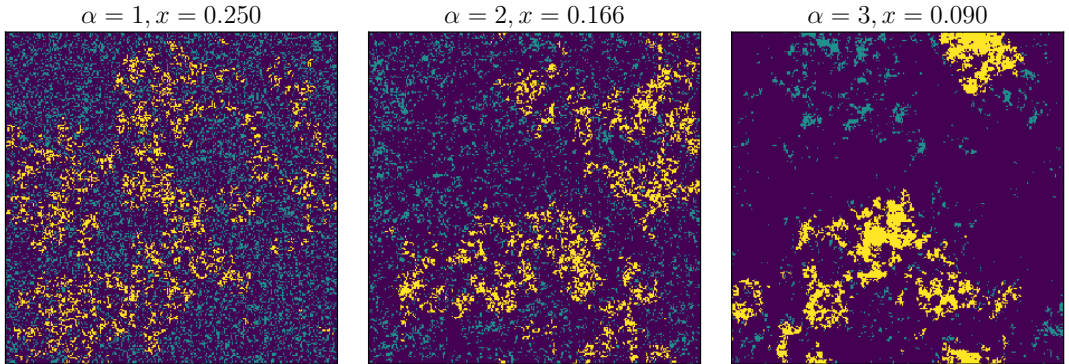


Figure 4.1. Two-dimensional slices from binarized realizations of GRFs shown at filling fractions $x = 0.250, 0.166$ and 0.090 (from left to right). Empty cells are shown in purple, cells belonging to the percolating cluster are shown in yellow, and all other occupied cells are shown in turquoise. The slices shown contain the largest number of cells within the respective percolating clusters.

4.2 Results and discussion

4.2.1 Order parameter and cluster number density

We calculate the order parameter for Gaussian random fields on a 256^3 lattice with various power spectra. A generated field $X(\mathbf{t})$ is binarized by considering the excursion set, F_x , at a threshold x_{th} chosen to match a given filling fraction x ; i.e. given $X(\mathbf{t})$ and a filling fraction, we calculate the threshold required such that setting the values at all points in the excursion set to one and all others to zero gives the desired average, x :

$$X(\mathbf{t}) \rightarrow \text{bin}\{X(\mathbf{t})\} = \begin{cases} 1, & \text{if } \mathbf{t} \in F_x. \\ 0, & \text{otherwise.} \end{cases} \quad (4.7)$$

We then consider all cells valued 1 as filled and 0 as empty.

Recall, the excursion set contains all the points in a field with value above a certain threshold. For fields with symmetric distributions, like a Gaussian field, the excursion set and its complement are statistically equivalent at reflected thresholds (reflected about the mean). Therefore, the order parameter as a function of filling fraction is identical in both cases. We can thus use the order parameter to gain insight into any non-Gaussian behaviour (or generally asymmetric behaviour) of a random field by examining deviations from this symmetry. We will see how the asymmetry of the ionization field manifests this way in the next chapter.

Here we present the results for three different Gaussian fields with power spectra going as power laws in k , $P(k) = k^{-\alpha}$, for exponents $\alpha \in \{1, 2, 3\}$ (see Figures 4.1 and 4.2). Diverging power spectra, e.g. $P(k) = k^{-\alpha}$ with $\alpha > 0$, are formally meaningless, but produce pure noise using a discrete

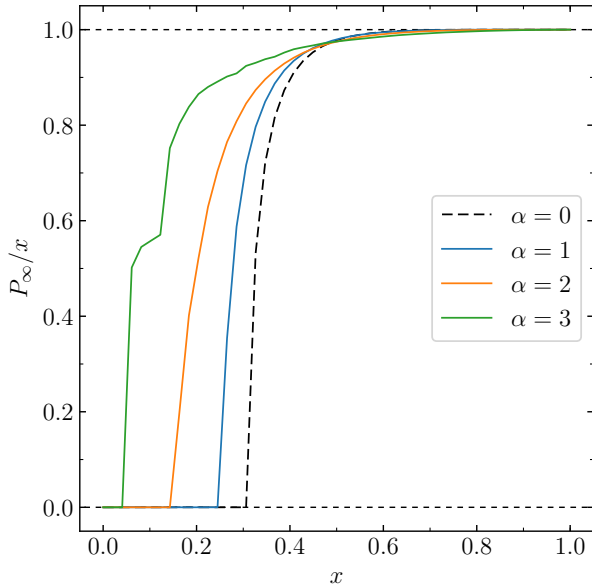


Figure 4.2. Order parameter for Gaussian random fields on a box of size 256^3 , with power spectra $P(k) = k^{-\alpha}$ for $\alpha \in \{0, 1, 2, 3\}$; where $\alpha = 0$ (dashed black) is the result from Section 3.1.3 corresponding to an uncorrelated field. The critical fractions, for increasing α , are 0.306, 0.245, 0.143, and 0.041.

Fourier transform, just like a constant power spectrum does. The result from Section 3.1.3 for uncorrelated (purely random) percolation³ is shown in dashed black in Figure 4.2.

Figure 4.1 shows slices of these fields at filling fractions chosen slightly above the respective critical fractions, and such that there are roughly the same number of cells shown in the percolating cluster across the three cases (~ 5000 cells). The stronger clumping of cells can be seen as more power is given to longer range correlations. Note that although the highlighted clusters do not seem to percolate the slice, they do percolate in the full 3d box.

The critical fractions, for increasing α , are $x_c = 0.306$ (uncorrelated), 0.245, 0.143, and 0.041. With more power in the correlations at low frequencies (large scales in real space) the critical fraction decreases significantly. This is because the growth and merging of clusters is aided by long range correlations, such that a single cluster can connect distant cells, and therefore percolate, even at a low filling fraction. The percolation transition seems to also become gentler as α is increased, due to stronger clumping of clusters which merge steadily throughout a wider range of filling fractions. For $\alpha = 3$, clipping can already be seen. Similarly, for values of α below three (not shown here) the data becomes

³This is equivalent to a Gaussian random field with a flat power spectrum, i.e. $\alpha = 0$, since its Fourier transform gives a Dirac delta as the correlation function; $\rho(\tau) = FT^{-1}[const.] \propto \delta(\tau)$, meaning uncorrelated points. The fact that the numbers are Gaussian-distributed rather than uniformly distributed has no implications on the order parameter as a function of filling fraction.

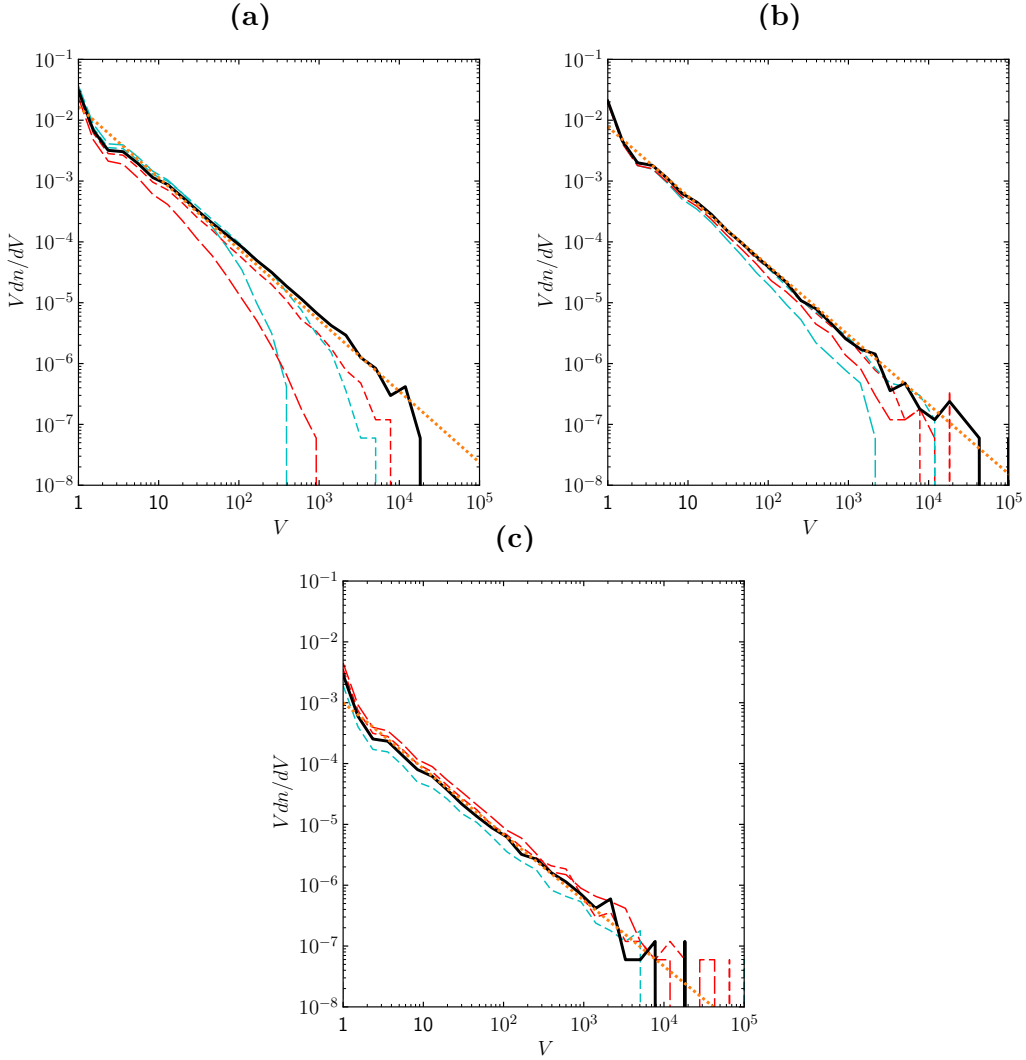


Figure 4.3. Cluster number densities for the same fields described in Figures 4.1 and 4.2; (a), (b), (c) correspond to $\alpha = 1, 2, 3$. The curves represent the distributions at the critical fraction (black), and at two values slightly above (dashed cyan) and slightly below (dashed red) this fraction, as well as the best-fit power law scaling (dotted orange). Bins at $V > 10^5$ with single counts are omitted from the figures.

highly distorted. In these cases, the box size needs to be increased in order to see the true percolation process. On average, all simulations with $\alpha \geq 3$ reach the same limit in the critical fraction, with increasing levels of scatter however. In theory, with $L \rightarrow \infty$, x_c would approach zero as the correlation range increased to infinity and all points became perfectly correlated.

The cluster number densities for these fields are shown in Figure 4.3 at their respective critical fractions, as well as at filling fractions $x = x_c \pm 0.02$ and $x = x_c \pm 0.06$. The power law scaling, $dn/dV \propto V^{-\tau}$, at the critical fraction is once again apparent, with exponents $\tau = 2.17, 2.14$, and 2.08 , for increasing α . These are all very close to the scaling in uncorrelated percolation (where

$\tau = 2.16$). Only for $\alpha = 3$ is there any significant change ($> 1\%$). We thus find that correlations do not manifest themselves distinctively in the scaling exponent τ . Instead, what can certainly be seen is that the dependence on $|x - x_c|$ is less pronounced. The stronger the long range correlations, the weaker the dependence of the cutoff scale on the distance to the critical fraction. This makes sense because the correlations which make it easier to form clusters of large volumes exist at all filling fractions and these begin to dominate the critical behaviour of the model.

4.2.2 Minkowski functionals

The Minkowski functionals for isotropic Gaussian random fields⁴ have known analytic expressions in any dimension, for any correlation function (Schmalzing & Buchert, 1997). They can be written in terms of a single parameter, λ , given by the second derivative of the correlation function evaluated at zero:

$$\lambda := \sqrt{\frac{|\rho''(0)|}{2\pi}}, \quad (4.8)$$

which can be calculated from the variance in any of the field's first derivatives, $|\rho''(0)| = \langle (\partial_i X(\mathbf{t}))^2 \rangle$.

In three dimensions, the expressions for V_k as a function of threshold are

$$V_0(x_{\text{th}}) = \frac{1}{2} - \frac{1}{2}\Phi\left(\frac{x_{\text{th}}}{\sqrt{2}}\right) \quad (4.9)$$

$$V_1(x_{\text{th}}) = \frac{2}{3}\frac{\lambda}{\sqrt{2\pi}} \exp\left(-\frac{x_{\text{th}}^2}{2}\right) \quad (4.10)$$

$$V_2(x_{\text{th}}) = \frac{2}{3}\frac{\lambda^2}{\sqrt{2\pi}} x_{\text{th}} \exp\left(-\frac{x_{\text{th}}^2}{2}\right) \quad (4.11)$$

$$V_3(x_{\text{th}}) = \frac{\lambda^3}{\sqrt{2\pi}} (x_{\text{th}}^2 - 1) \exp\left(-\frac{x_{\text{th}}^2}{2}\right), \quad (4.12)$$

where $\Phi(x)$ is the error function, given by

$$\Phi(x) = \frac{2}{\sqrt{\pi}} \int_0^x e^{-t^2} dt. \quad (4.13)$$

We calculate these using the algorithm by Schmalzing and Buchert (1997). Due to clipping and other unknown errors in the implementation we have of their code, we calculate V_0 separately (recall this is simply the volume of the excursion set, or the filling fraction of percolation theory) and significantly scale and stretch the analytic expressions for the other three MFs to match

⁴We consider fields with mean zero and variance one, as before, without any loss of generality.

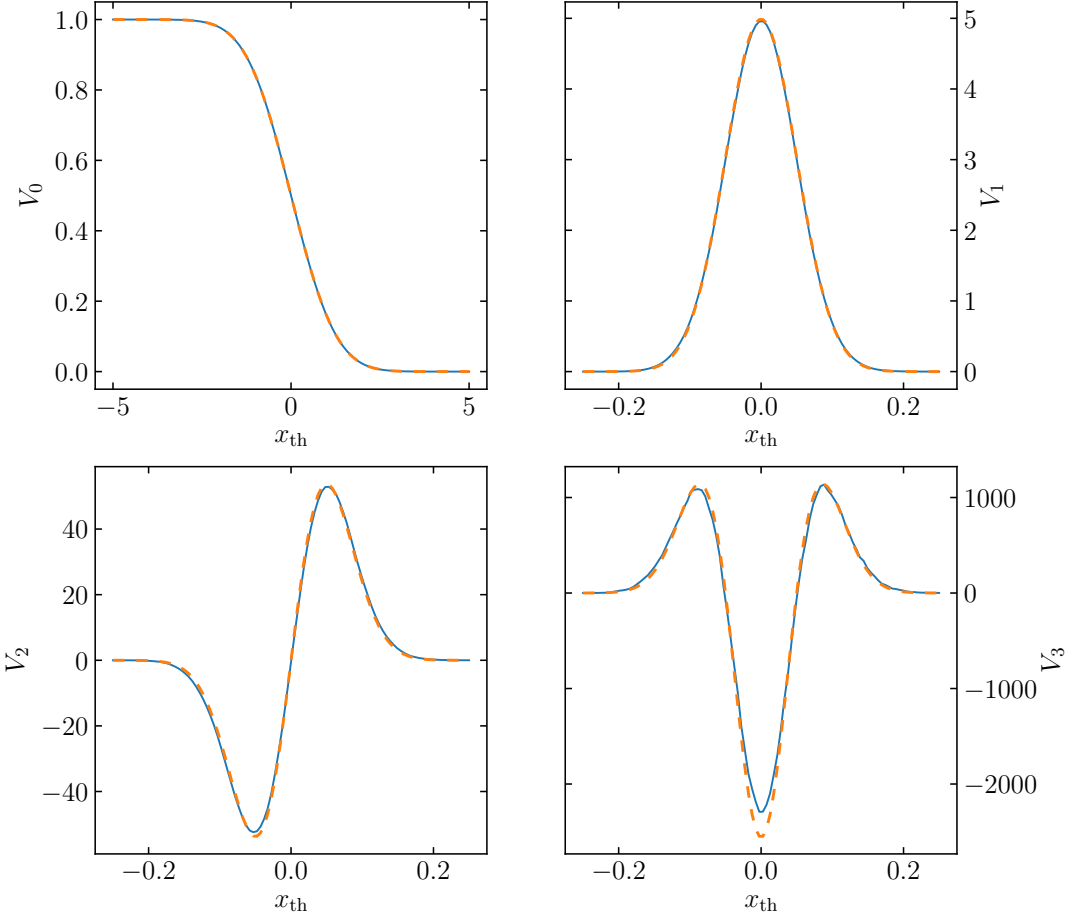


Figure 4.4. Minkowski functionals for a 3d Gaussian field with a wide Gaussian power spectrum. The blue curves are the calculated results. The orange dashed curves are the analytic expressions after heavy scaling and stretching. For the last three MFs, the analytic curves were scaled to $65 \cdot V_1(20 \cdot x_{\text{th}})$, $4 \cdot 10^3 \cdot V_2(20 \cdot x_{\text{th}})$ and $4 \cdot 10^5 \cdot V_3(20 \cdot x_{\text{th}})$, respectively.

the data. In any case, as mentioned previously, we are only interested in relative values, although fixing this problem in the future would increase our confidence in these results. The MFs shown in Figure 4.4 are for Gaussian noise on a 128^3 lattice, smoothed (i.e. convolved) with a Gaussian of mean zero and standard deviation two. This is equivalent to a Gaussian field with a wide Gaussian power spectrum, as can be seen from eq. (4.6)⁵. The data is practically indistinguishable from the analytic expressions, except at the minimum in V_3 . Minkowski functionals demonstrate the symmetry of a GRF in that they are all themselves symmetric.

⁵A convolution in real space becomes a multiplication in Fourier space, and the Fourier transform of a Gaussian is another Gaussian with standard deviation $\sigma' \propto 1/\sigma$.

The maximum in surface area appears when half the cells are filled, while the same point appears as a minimum in the Euler characteristic (V_3). At $V_0 = 1/2$ there is also a zero in V_2 , meaning that (on average) the curvature is saddle-like. The extrema in V_2 occur at the zeros of V_3 , as can be seen by differentiating the expression in eq. (4.11).

Consider the zero in V_3 at positive threshold: the filling fraction is very low so the number of cavities is likely to be negligible. Therefore, this value occurs when the number of parts balances the number of tunnels, and the genus is closest to zero, meaning there is probably a single filamentary structure which dominates the lattice with about as many tunnels as there are other isolated parts (or the lattice is filled with regions that have folded into the topology of single-holed tori in isolation, which seems like a very special scenario). The same can be said for the zero at negative threshold, with parts and cavities exchanging roles. [Mecke and Wagner \(1991\)](#) suggested that a zero in the Euler characteristic corresponds to a critical filling fraction in the order parameter. A second critical fraction would then represent percolation in the complement of F_x . They tested this statement for various percolation models in two and three dimensions and found a compelling consistency in the results. We return to this idea in our discussion of reionization.

4.2.3 Granulometry

Granulometric sieving on the fields discussed above picks up very little information, since the shapes of the clusters are not well described by overlapping spheres. For the case of power law correlations, the largest spheres which fit into clusters (even at 80% filling, when $\alpha < 3$) are only a few cells in radius, $R_{\max} \sim \mathcal{O}(1) \sim 1\text{--}2\%$ of the lattice size. Only for $\alpha = 3$ at $x = 0.8$ does the largest sphere reach a radius $R_{\max} = 16/256 \approx 6\%$ of the lattice size. Power law correlations create highly porous clusters which contain many tunnels and cavities at all filling fractions, and thus sieving with solid spheres is inadequate. Similarly, the field described in the previous section, with noise smoothed over two cells, has $R_{\max} = 6$ when realized on a larger lattice of 256^3 cells at $x = 0.5$. In this case, the clusters do not contain many cavities but are highly filamentary, such that they are also misrepresented by spheres as structuring elements.

Therefore, we apply the technique to the power law fields after smoothing over two cells. This fills holes in the clusters while maintaining the clumping produced by power law correlations. The results are plotted in Figure 4.5.

We observe a cutoff in the distribution which increases with α , as is expected. Also, a characteristic size appears in the distributions at $R = 4$ for both $\alpha = 1$ and $\alpha = 2$, and at $R \sim 8$ for $\alpha = 3$. This is partly due to the Gaussian smoothing which removes almost all features of $R \leq 2$ and most features of $R \leq 4$. We see that many features of larger size exist in the clusters, but are broken by empty voids of a few cells in size when unsmoothed. When

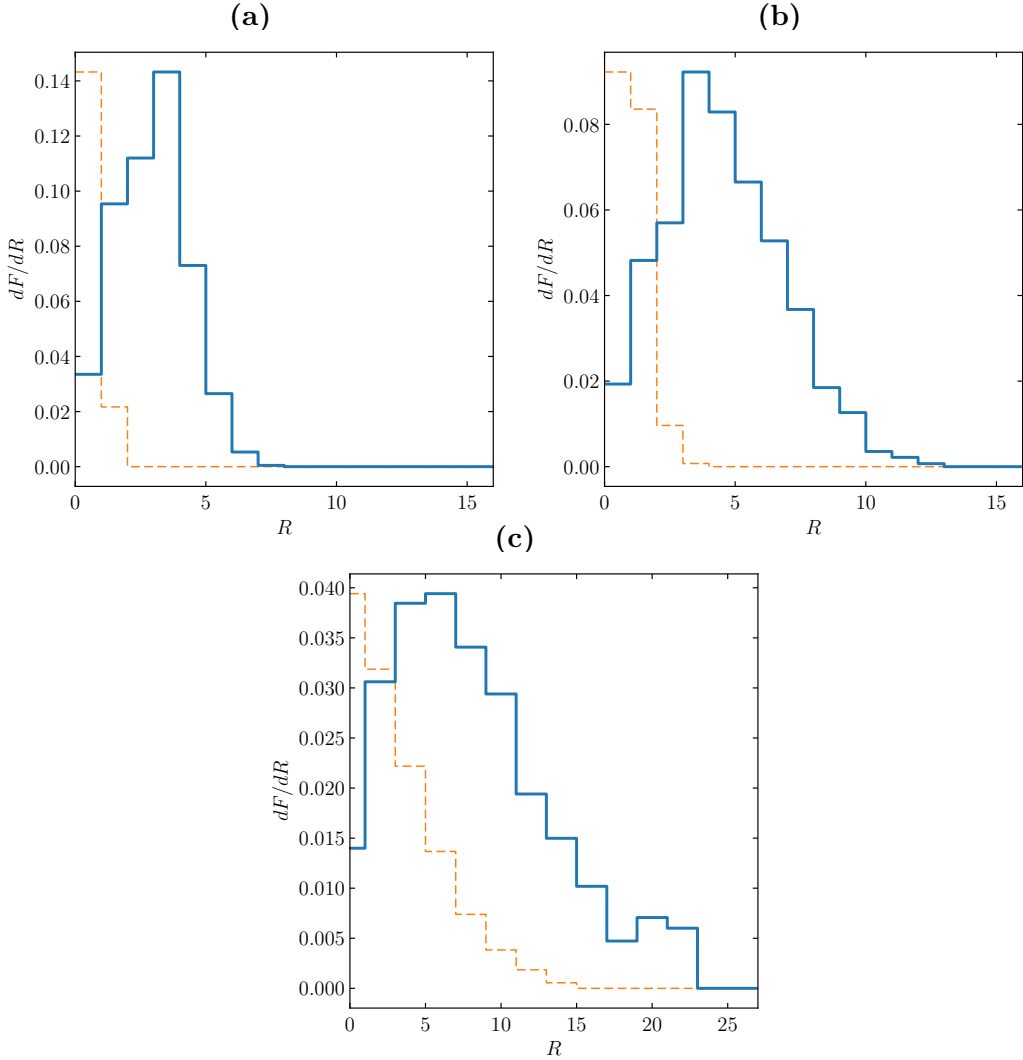


Figure 4.5. Granulometric size distributions for Gaussian fields with power law correlations, generated on a 256^3 lattice. (a), (b), (c) correspond to $\alpha = 1, 2, 3$. In blue, the distributions after smoothing by two cells at a filling fraction of 0.5; in dashed orange, the distributions for the original fields at a *higher* filling fraction of 0.8. The data for $\alpha = 3$ is binned every two cells in radius to reduce noise. At $x = 0.5$, granulometry on the unsmoothed fields gives close to no data (not shown). Notice how smoothing by only two cells is enough to fill the holes breaking features which are otherwise much larger.

setting $\alpha = 3$, the correlations become strong enough to form solid bubbles of size $R \gtrsim 20$ cells at half filling, each contributing to about 8% of the lattice.

CHAPTER 5

Reionization, heating and cooling

We are now ready to analyze the percolation processes which occur during cosmic reionization and the preceding phases of heating and cooling.

Simulated data of the 21 cm signal is produced using the semi-numerical tool called 21cmFAST ([Mesinger et al., 2011](#)). *Semi*-numerical because it uses approximate physics to evolve the underlying fields, but is capable of independently generating full three-dimensional realizations of the data; its output includes separate component maps of the underlying fields. Such tools are incredibly useful when examining the large-scale evolution of the Universe. They allow for an exploration of vast parameter spaces and simulation boxes spanning hundreds of megaparsecs in width. This is completely unachievable with full radiative transfer simulations, which require many months to complete realizations on the order of 100 Mpc^3 in volume on expensive supercomputer clusters. 21cmFAST is faithful to these simulations at scales $\gtrsim 1 \text{ Mpc}$ and can run through a wide range of redshifts in a matter of days.

We use two sets of 21cmFAST boxes provided by Dr. Pritchard, containing 256^3 cells and spanning 300 Mpc^3 in volume, i.e. with a resolution of $1.17 \text{ Mpc}/\text{cell}$. The first simulates redshifts $6 \leq z \leq 12$ and ignores the spin temperature contribution to the 21 cm brightness temperature. These redshifts correspond to reionization and here we focus specifically on the evolution of the ionization field. The second simulates $6 \leq z \leq 34$ and accounts for fluctuations in the spin temperature, as these become the prevailing component of δT_b at higher redshifts. Here, we consider the heating and cooling stages which occur at redshifts $11 \lesssim z \lesssim 16$ and $16 \lesssim z \lesssim 25$, respectively. We discuss these three phases mostly in the bulk, but no sharp boundaries exist between them and there are transition periods which would require more careful attention. Since our analysis applies to a limited set of 21 cm realizations, our results depend on the specific model we have used. However, many of the conclusions drawn are not unique to this work and can be considered more general. An investigation into the robustness of newer conclusions with respect to changes in physical parameters is left to future works.

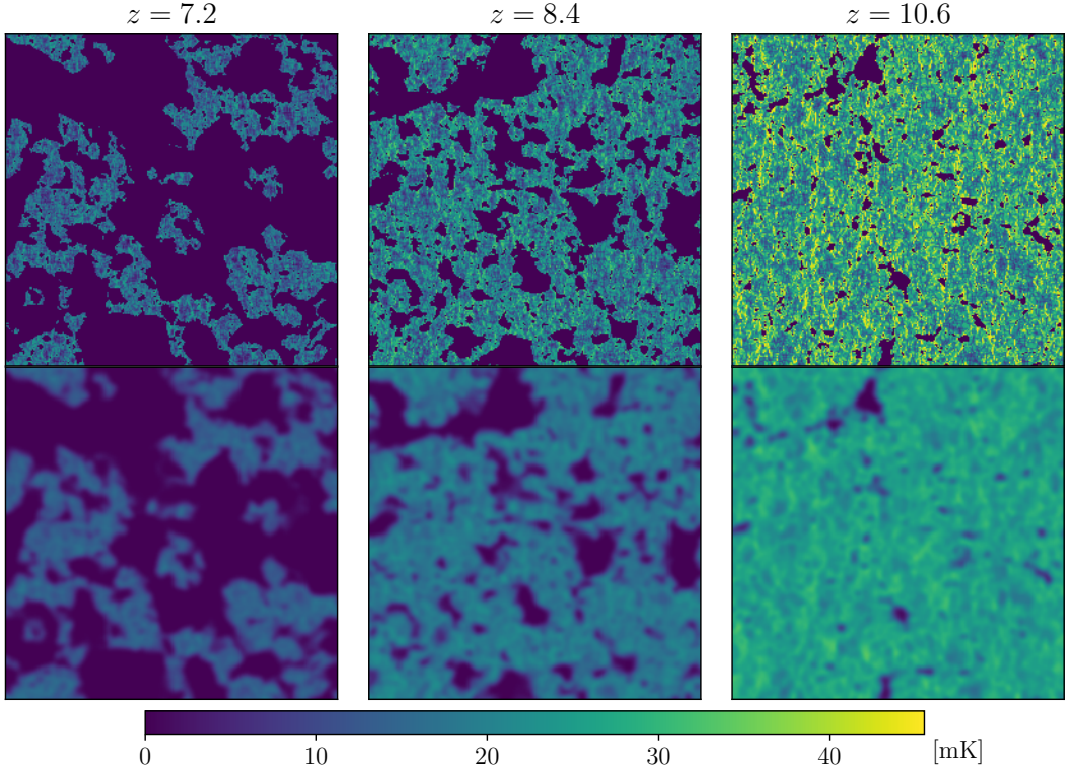


Figure 5.1. Slices from the simulation box at redshifts $z = 7.2, 8.4$ and 10.6 , shown before and after smoothing by two cells (top and bottom, respectively). Note that the fully ionized cells ($\delta T_b = 0$) percolate in $3d$ at all shown redshifts.

5.1 Reionization

5.1.1 Order parameter for reionization and its reverse process

The order parameter at fixed threshold

Simulating the ionization field with 21cmFAST produces cells with varying degrees of ionization. In reality a hydrogen atom is either ionized or neutral, however cells representing volumes of one cubed megaparsec in a simulation could contain many atoms of both kinds. 21cmFAST models this with partially ionized cells, therefore we need to fix a threshold to binarize its output. Example visualizations of the produced 21 cm brightness temperature are shown in Figure 5.1 at redshifts $z = 7.2, 8.4$ and 10.6 . The purple cells are fully ionized; low brightness cells could be either highly ionized or under-dense and mostly neutral regions; high brightness cells are neutral and over-dense. Smoothed versions of the boxes are also shown as these are useful in evaluating Minkowski functionals. Such an effect could also correspond, for example, to the limited resolution of a telescope. We will consider percolation in the underlying ionization field.

Figure 5.2 shows the order parameter calculated for both the ionized and neutral media. Percolation in the latter can be considered as a (time-reversed) process of reconstruction of a fragmented neutral medium. We binarize the ionization field such that the global ionized fraction does not change under the transformation. This amounts to treating all cells with an ionized fraction greater than or equal to $x_{\text{th},i} = 0.25 \pm 0.01$ as fully ionized (on average over the redshift range) or, equivalently, setting a similar threshold in the neutral fraction of $x_{\text{th},n} = 0.75 \pm 0.01$. For this plot, we use boxes with both 256^3 cells (result shown in dashed orange) and an additional set of boxes with 512^3 cells spanning 600 Mpc^3 (shown in blue), i.e. with the same resolution but simulating a larger volume of space. The redshifts are sampled in equal increments of $\Delta z = 0.2$ and hence we have better resolution of percolation in the ionized medium, at low global ionized fraction (higher redshifts), than in the neutral counterpart (see Figure 2.1).

The critical ionized fraction is found to be $x_{i,c} \approx 0.1$, above which there is a rapid rise in the OP as the percolating cluster quickly absorbs all other clusters. By $x_i \approx 0.25$, more than 90% of the ionized volume is contained within this single cluster. This is much lower than the critical fraction for random percolation and comparable to strongly correlated Gaussian fields. Neutral cells in the neighbourhood of ionized regions are highly likely to become ionized in the next time step. The correlations imposed by the inside-out growth of ionized regions, rather than a random sprinkling of ionized cells, allows an infinite cluster to form at this very low filling fraction. The difference between the 300 Mpc^3 and 600 Mpc^3 realizations is entirely negligible, confirming that we are not mistaking a large (finite) cluster as the percolating cluster.

Calculating the OP for H I, we find that the result is not a mirror image of the OP for H II. Regardless of the coarser sampling, this asymmetry gives us information about the differences in the correlations and distribution of the two media. In the neutral medium, we find that a percolating cluster appears at a critical fraction $x_{n,c} \approx 0.05$ (and less than 0.087). A lower value than $x_{i,c}$ suggests that there could be shielding effects in H I which prevent the neutral percolating cluster from breaking until a later stage compared to its ionized analogue. Also, we have $P_\infty = x_n$ for all neutral fractions $x_n \gtrsim 0.2$, while P_∞ for the ionized gas gradually approaches x_i . This could be due to the limited reach of ionizing sources caused by IGM absorption and to the emergence of isolated ionized bubbles throughout reionization, surrounding new galaxies born out of the neutral IGM.

The intermediate period between $x_i \approx 0.1$ and $x_i \approx 0.95$ can be thought of as an *overlap phase*, during which unique percolating clusters exist in both the ionized and neutral gases (Furlanetto & Oh, 2016). These intertwine with each other until one becomes large enough that the other fragments into smaller pieces. The *pre-overlap* and *post-overlap* phases then describe the periods when a single percolating cluster exists in either the neutral medium or the ionized medium, respectively.

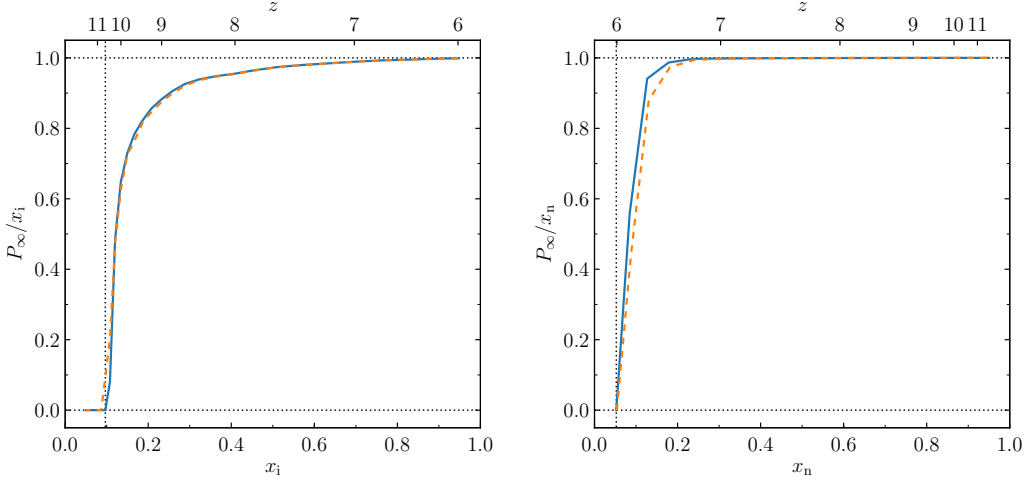


Figure 5.2. Order parameter for percolation in the ionized (left) and neutral (right) IGM. The blue curve shows the result in a 600 Mpc^3 box with 512^3 cells, and the dashed orange curve shows the result for a 300 Mpc^3 box of the same resolution.

Dependence on threshold

The shape of the order parameter depends on the threshold chosen to binarize a field. Since we do not resolve the true ionization fronts, one could consider, for example, percolation of only the fully ionized regions, or regions with at least half of their volume being ionized (as is often the case in the literature). The order parameter for thirty evenly spaced thresholds, as a function of redshift, is shown in Figure 5.3 for the ionized and neutral processes. Yellow corresponds to an OP of one and purple to an OP of zero.

Clearly, lower thresholds allow percolation to occur earlier, and at low enough values we begin to connect to mostly neutral clusters. However, we see that the dependence flattens out above $x_{\text{th},i} \approx 0.25$, which is the average threshold in Figure 5.2. There are few partially ionized cells and the plot agrees with the expectation that these add little to the connections between clusters. Thresholds above this value give mostly consistent results.

At the current redshift spacing, we are not able to resolve any dependence on threshold for percolation in the neutral gas, except that considering only fully neutral cells slightly underestimates the duration of the overlap phase. We expect the curve to remain mostly flat, as in the case of H II, for reasons which will become clear when discussing Minkowski functionals.

By examining the 21 cm brightness temperature field during reionization, we find that the signal below $\delta T_{\text{th}} \approx 10 \text{ mK}$ maps the percolation of ionized hydrogen very well. Figure 5.4 shows the order parameter of the brightness temperature field when considering all cells with $\delta T_b \leq \delta T_{\text{th}}$ as filled. Neutral cells seem to only come into play at temperatures above 10 mK , and the density fluctuations do not seem to alter the shape of the order parameter for the ionized gas. This is likely because the clustering of ionizing sources is strongly

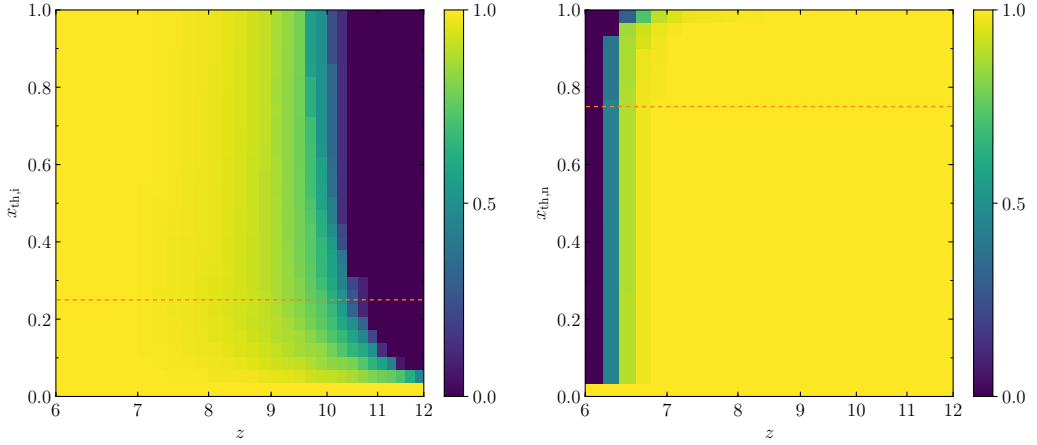


Figure 5.3. Order parameter of the ionization field as a function of redshift for various binarizing thresholds. Ionized gas is considered in the left plot and neutral gas on the right. The red dashed lines represent the average threshold chosen in producing Figure 5.2.

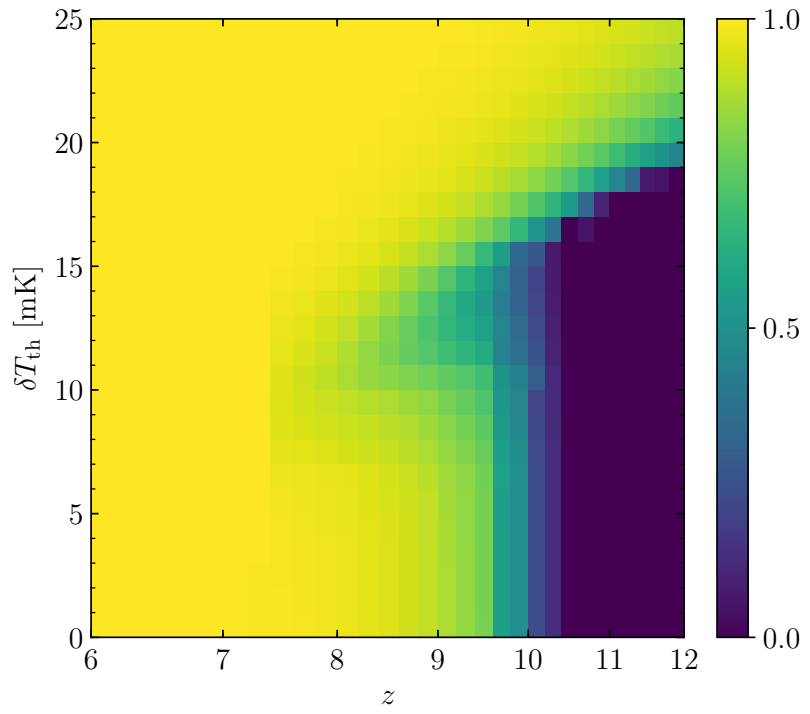


Figure 5.4. Order parameter of the 21 cm brightness temperature field at various thresholds. Cells with value below a given threshold are considered filled, in order to map the distribution of H II.

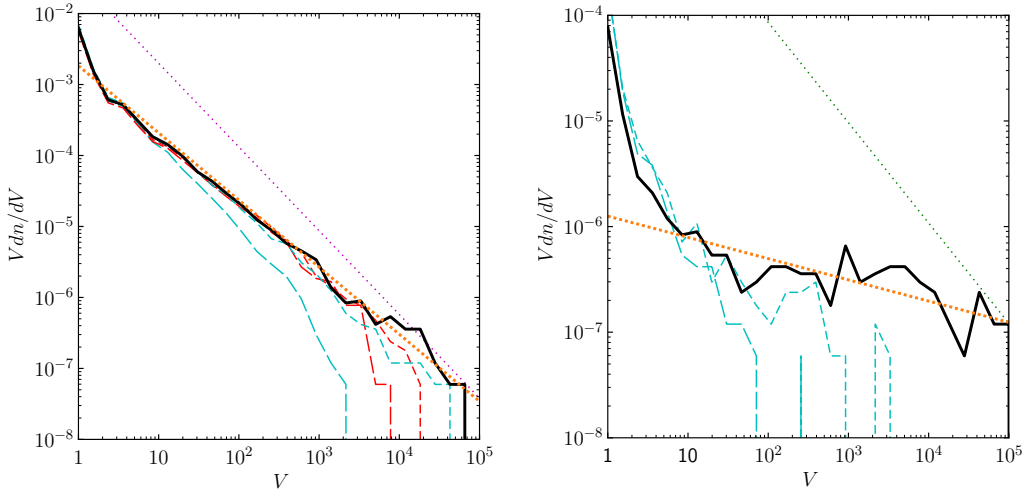


Figure 5.5. Cluster number density in the ionized (left) and neutral (right) media. The distributions are shown at the respective critical fraction (black), slightly above it (dashed cyan), and for ionized hydrogen also slightly below it (dashed red). The dotted orange lines show the power law scaling $dn/dV \propto V^{-\tau}$ with exponent $\tau = 1.95$ for H II and $\tau = 1.20$ for H I. The scaling for random percolation ($\tau = 2.19$) is shown in the left plot (dotted magenta); while the scaling for ionized hydrogen ($\tau = 1.95$) is shown on the right (dotted green). Volumes above 10^5 cells have single counts and are not shown (this includes the percolating cluster).

coupled to the location of over-densities and thus the latter are already accounted for in the order parameter of the ionization field. In the following subsections we examine the morphology and topology of the ionization field and return to the full brightness temperature when discussing heating and cooling.

5.1.2 Size distributions in the ionization field

We calculate the cluster number density as a function of volume for the ionized and neutral regions of our 256^3 box near the respective critical points. The field is binarized at a fixed threshold as discussed at the start of this section and the results are shown in Figure 5.5.

In H II, the power law behaviour, $dn/dV \propto V^{-\tau}$, is evident over a wide range of volumes, with a scaling exponent $\tau = 1.95$. This is lower than all random models previously discussed and shows the preference towards larger ionized clusters. The curves above the critical fraction are shown at $x_i \approx 0.12$ and 0.23 (dashed cyan); below, they are shown at $x_i \approx 0.06$ and 0.05 (dashed red). As expected, these follow the power law up to a cutoff scale which decreases as the distance to $x_{i,c}$ increases.

In H I, the scaling is less clear. We attempt to fit a power law to the distribution at volumes larger than 10 cells and find these scale roughly to $\tau = 1.20$. However, there is evidently more weight at lower volumes than a power law would suggest. This remains the case at neutral fractions above

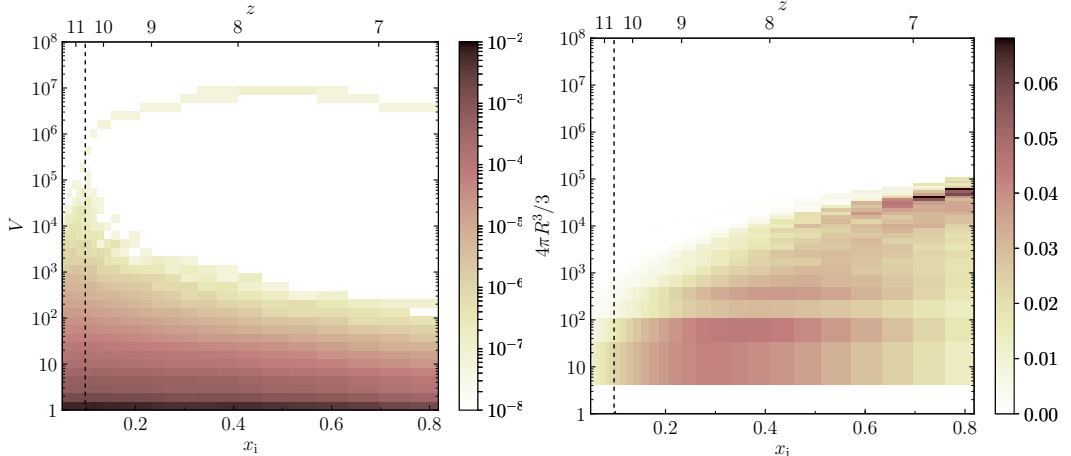


Figure 5.6. Cluster number density (left) and the granulometric size distribution (right) of ionized regions as a function of redshift or filling fraction. Radii for granulometry are scaled to the corresponding sphere volumes. The vertical dashed lines represent the critical fraction $x_{i,c} \approx 0.1$.

the critical fraction. We plot the curves at $x_n \approx 0.24$ and 0.49 (dashed cyan). At these fractions, the distribution represents the tiny extra neutral volume disconnected from the percolating cluster and living in cavities of the ionized IGM. Clusters of intermediate volumes appear less prevalent than small clusters compared to the ionized medium.

The evolution of the cluster number density and the size distribution obtained with granulometry are shown in Figure 5.6. The number density clearly shows a break in the distribution at the critical fraction. Above this point, the number density evolves in two segments: a single large percolating cluster which continues to grow, and the remaining distribution which gradually shrinks. The cutoff in the volume of isolated regions decreases as the percolating cluster eats away at the curve. It is also apparent that no characteristic cluster volume exists (at any ionized fraction). An anomalous breaking of the percolating cluster occurs near $x_i \sim 0.6$. This cannot be the case for the true percolating cluster, however, and must be due to our code.

Granulometry describes the scaling of spherical features in the ionization field. Remember that above the critical filling fraction the ionized volume is almost entirely contained in the percolating cluster, so the features we identify are of the percolating cluster itself. At $x_i < x_{i,c}$ the existing scales are very small as the clusters have not merged into larger bubbles. The transition to percolation is much less evident since there is no real change in the shape of clusters at this point. The small-scale features of the percolating cluster are dominant until $x_i \sim 0.3$, at which point over 95% of the ionized IGM is in the percolating cluster. As more gas is ionized, the cluster becomes less filamentary and larger sized features grow more common. This continues until the IGM contains very few and sparse neutral pockets, around $x_i \sim 0.7$.

5.1.3 Minkowski functionals and their relation to percolation

The Minkowski functionals of the ionization field provide highly condensed and valuable insight into the topology of reionization and are closely related to the order parameter. We calculate these after smoothing our boxes over two cells. This does not change the general shape of the MFs, but rather makes their features clearer by removing sharp ridges. On the other hand, smoothing tends to sharpen the transition in the order parameter, while also obviously strengthening its dependence on threshold. However, this does not significantly affect $x_{i,c}$. We also oversample the field by two cells, meaning we take values from the original grid and interpolate them onto a sub-grid of twice the resolution. This further improves the quality of the data by ensuring that connections between filled cells are treated equally to those between empty cells. Thus, the symmetries in the Minkowski functionals (discussed previously) for an excursion set and its complement are more closely met. Oversampling does not strongly affect the order parameter as, unlike smoothing, it does not fill in small holes or remove any small features¹.

Figures 5.7 to 5.10 show the full results obtained for the Minkowski functionals at all redshifts. These can be interpreted both in the usual sense: at fixed redshift as a function of threshold; and in the percolation sense: with a fixed threshold and variation in time. In all plots, the red scale represents positive values, the blue scale negative values, and white represents zero. The values at $x_{\text{th},i} = 0$ are omitted due to unstable points at low redshifts. All the MFs are zero in this case, except for V_0 which is of course one. Figure 5.11 shows line plots stripped from these results at redshifts $z = 7.6$ (blue), 8.4 (purple), 9.2 (red) and 10.4 (green).

The general features of the curves and their interpretation are direct analogues to the case of Gaussian random fields. We focus therefore on their evolution as reionization progresses and on relations to the order parameter. Contours of constant order parameter are overlaid onto Figures 5.7 to 5.10 for $P_\infty/x_i = 0.01, 0.50, 0.90, 0.95$ and 0.99 (recalculated for the smoothed boxes).

Volume and surface area

The general behaviour of V_0 is as one would expect. By comparing to the contour $P_\infty/x_i = 0.01$, we observe that although there is a strong dependence on threshold for the redshift at which percolation occurs, the critical ionized fraction varies very little with threshold. The contour $V_0 = 0.1$ (Figure 5.7, dotted black) follows the critical fraction well. The shape of the order parameter is consistent at all thresholds when understood as a function of filling fraction. This to be expected since all partially ionized cells obey the same correlations created by 21cmFAST’s flagging algorithm.

¹See Appendix C in [Friedrich et al. \(2011\)](#) for greater details on oversampling.

For V_1 we see a highly asymmetric curve, with most of the contributions coming from ionized cells. As reionization progresses, this becomes increasingly the case. The peak in V_1 for any given redshift (Figure 5.8, dotted black) corresponds to the minimum in V_3 , as was the case for Gaussian fields. It occurs when there is a balance in size between the neutral and ionized percolating clusters, i.e. the point of half filling ($V_0 = 0.5$), as expected. At high redshifts, a lower threshold is required to achieve this because there are few ionized atoms. As time goes on, $x_{\text{th},i}$ can be relaxed. We also see that in this finite lattice, the maximum in V_1 is related to the state with OP one, where all the ionized volume is in a single cluster.

Curvatures

The integral curvatures are also asymmetric, with a wider spread towards higher partial ionizations. The maximum in integral mean curvature (Figure 5.9, dotted black over red) appears to give an upper bound on the critical ionized fraction. The discrepancy is exacerbated when shown on a redshift scale, but the respective filling fractions are in fact very close. At high threshold values (above $x_{\text{th},i} \sim 0.4$), this maximum begins to shift away from the onset of percolation towards higher OP contours. For a threshold $x_{\text{th},i} \approx 0.25$, as was chosen in our original discussion of the order parameter, the maximum mean curvature occurs at a global ionized fraction $x_i \sim 0.2$, above the critical point $x_{i,c} \sim 0.1$. This is not an exact match, but the relationship between the percolation transition in the ionized medium and the maximum in V_2 is robust. Measuring such a maximum would signify that the transition towards H II percolation has begun and that an infinite cluster exists. At the same time, one can apply this reasoning to the minimum in V_2 . Percolation of the neutral IGM would therefore be tied to this point at thresholds above $x_{\text{th},n} \sim 0.6$.

The zeros in V_3 provide an even more convincing correlation to the order parameter. Figure 5.10 shows these in dotted black, while the extrema of V_2 are now shown in red (maximum) and cyan (minimum). The first zero point in the Euler characteristic is found to be an additional upper bound on the critical point of percolation. It corresponds perfectly to the maximum in V_2 in the redshift range $z \sim 9\text{--}11$. The Euler characteristic continues to mark the percolation transition at higher thresholds as well, but separates from the maximum in mean curvature. When considering only highly ionized cells, the zero in V_3 is found at $x_i \sim 0.15$. This is a good indication of the critical point. The second zero corresponds to the fall in the OP for neutral hydrogen. This curve is flat for most thresholds and thus we expect the order parameter for neutral hydrogen to follow a similar relationship. Positive values below this curve agree with the fragmentation of the neutral percolating cluster.

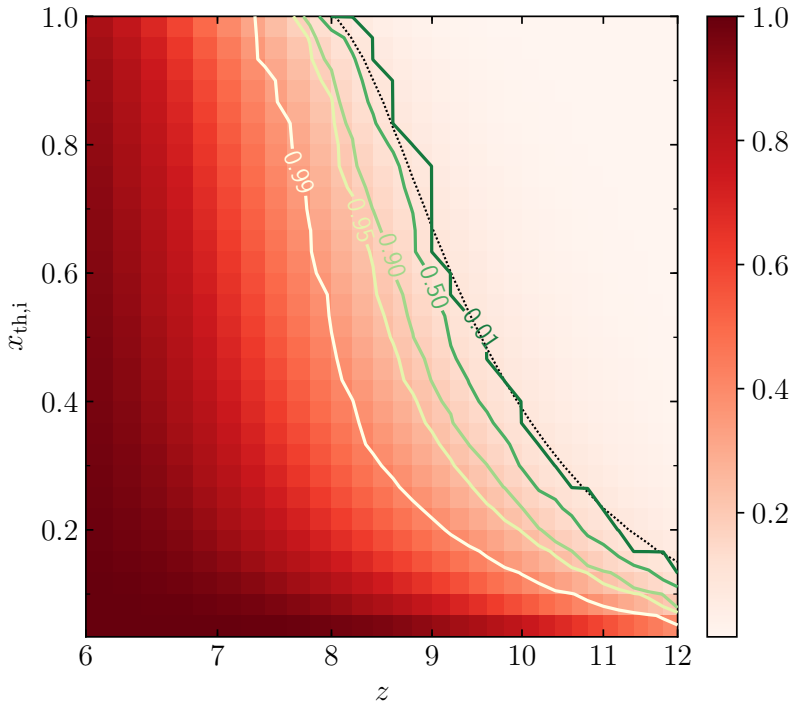


Figure 5.7. V_0 for the smoothed and oversampled ionization field. The contour for $V_0 = 0.1$ is shown in dotted black. The contours of constant order parameter are overlaid in shades of green. Note the color-coding for these is reversed compared to the subsequent figures to give better contrast.

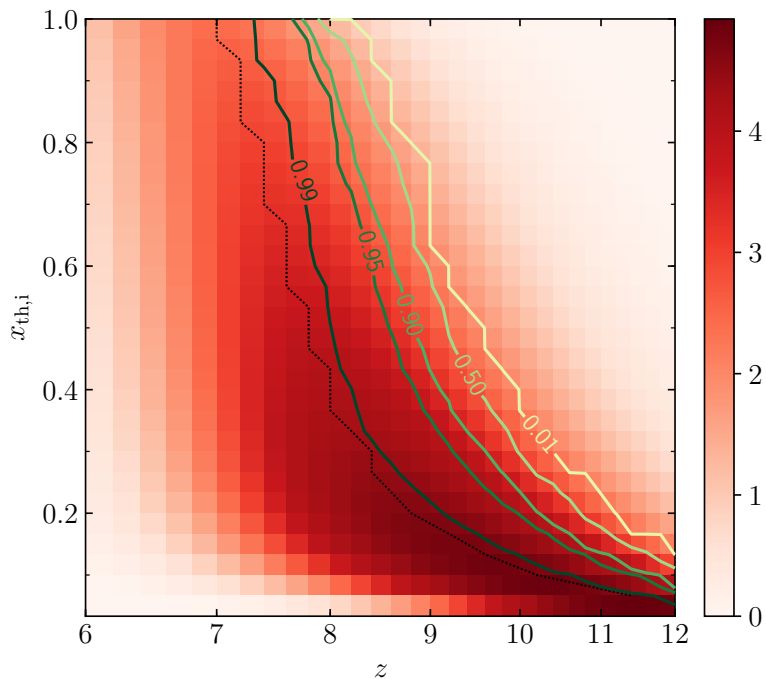


Figure 5.8. V_1 for the same. Here, the dotted black line highlights the maximum of $V_1(x_{th,i}; z)$ at any given redshift.

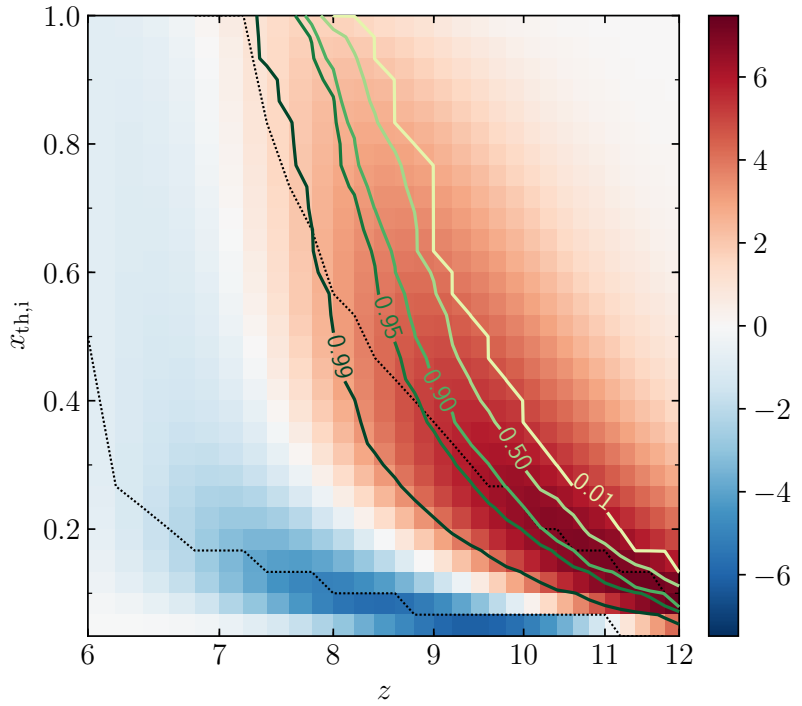


Figure 5.9. $V_2 \cdot 10^{-1}$ for the smoothed and oversampled ionization field. The maximum and minimum of $V_2(x_{\text{th},i}; z)$ are highlighted by the dotted black lines.

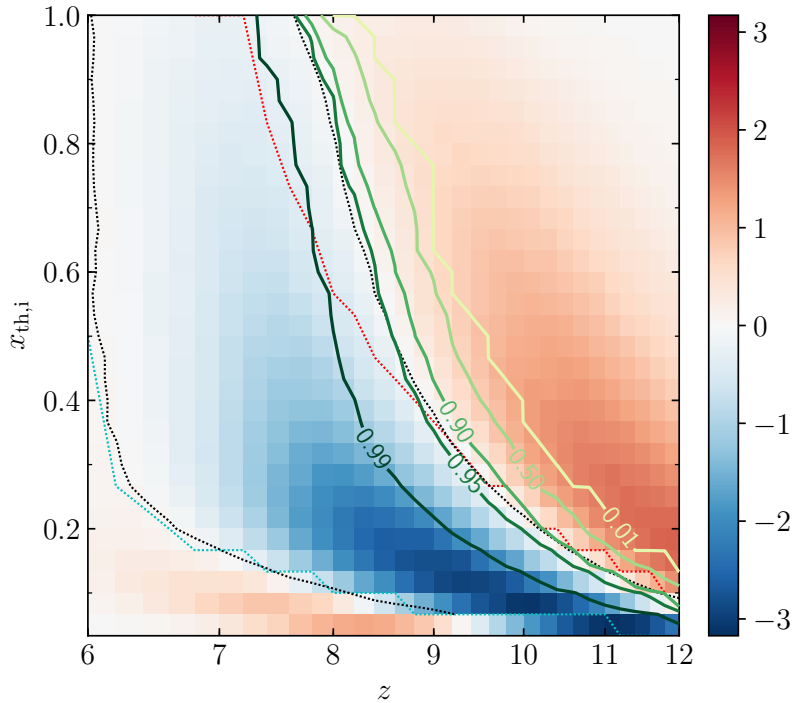


Figure 5.10. $V_3 \cdot 10^{-3}$ for the same. Here, the maximum and minimum of $V_2(x_{\text{th},i}; z)$ from Figure 5.9 are shown in dotted red and cyan, respectively, while the dotted black lines represent the zeros of $V_3(x_{\text{th},i}; z)$.

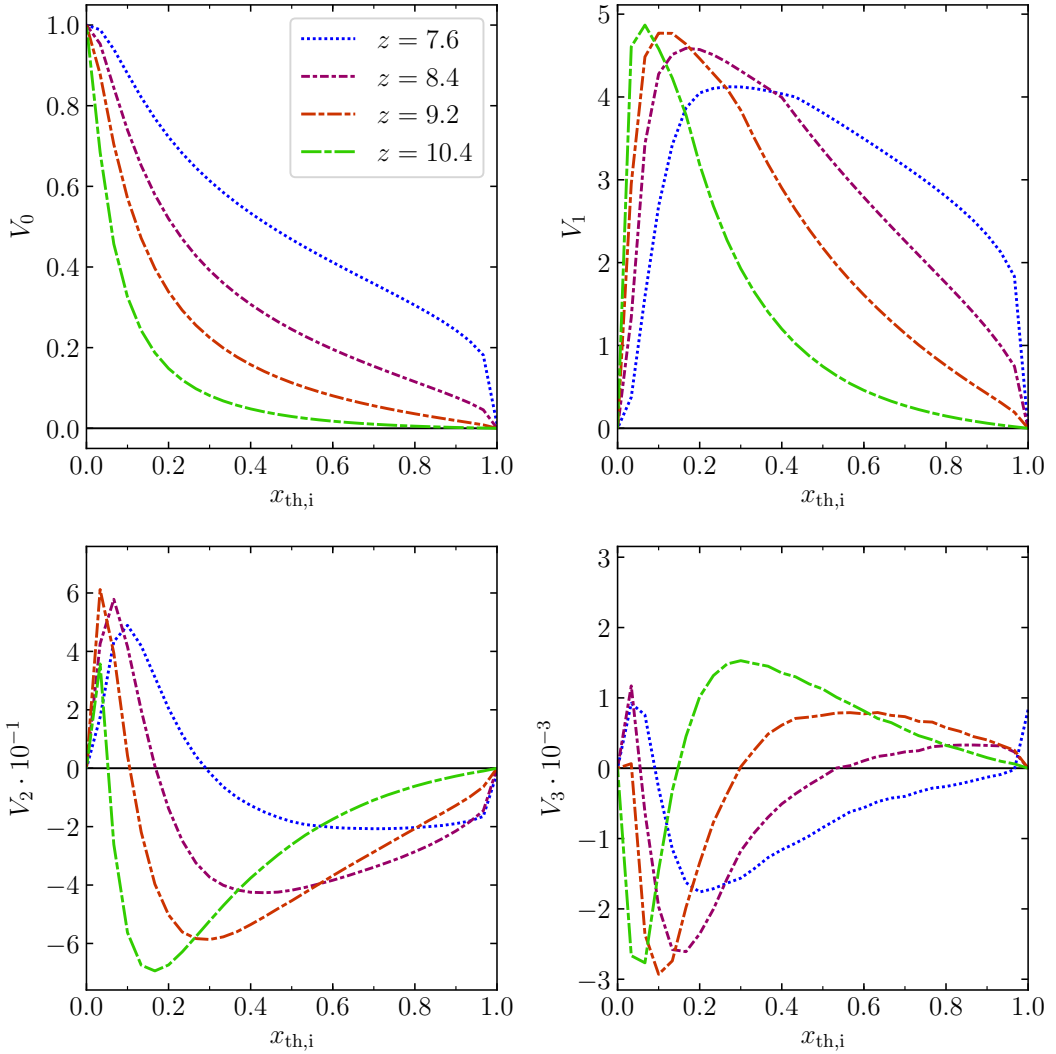


Figure 5.11. Line plots from Figures 5.7 to 5.10 at redshifts $z = 7.6$ (blue), 8.4 (purple), 9.2 (red) and 10.4 (green).

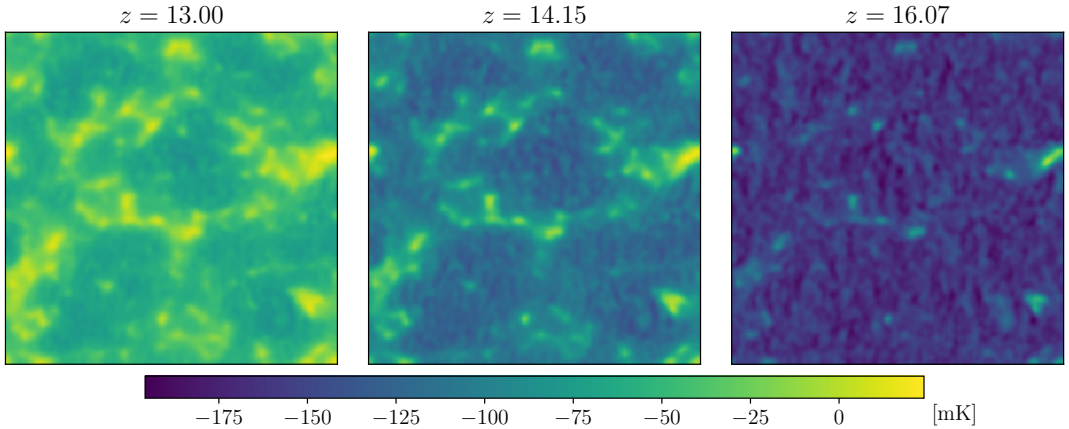


Figure 5.12. Slices from the simulation box including the spin temperature and smoothed over two cells. The boxes are shown at redshifts $z = 13.00$, 14.15 and 16.07 , corresponding to the heating phase. Notice how the change in mean temperature is much more evident than during reionization, while hot spots are still clearly formed. These are over-dense regions heating more rapidly than average.

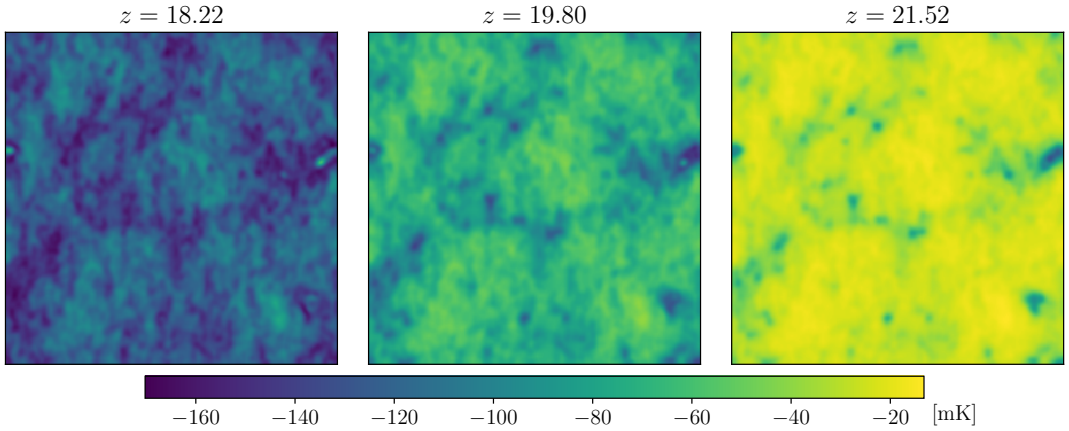


Figure 5.13. Slices from the same simulation at redshifts $z = 18.22$, 19.80 and 21.52 , corresponding to the cooling phase. Cold spots are more difficult to track by eye.

5.2 Heating and cooling

5.2.1 Order parameters for hot and cold gas

Before reionization, the 21 cm signal tracks the heating and cooling of the IGM, which enclose the era of first galaxy formation (see Figures 5.12 and 5.13). Substantial variation in the mean signal introduces a strong dependence of the order parameter on the threshold temperature chosen to binarize the signal. In fact, there is no single percolation process which can interpret its evolution across the full range of values. We therefore have percolation occurring at different moments in time for each temperature.

We calculate the OP over the redshifts $z \sim 9\text{--}17$ while considering the percolation of hot spots. A cell is considered hot if it has a temperature $\delta T_b \geq \delta T_{\text{th}}$.

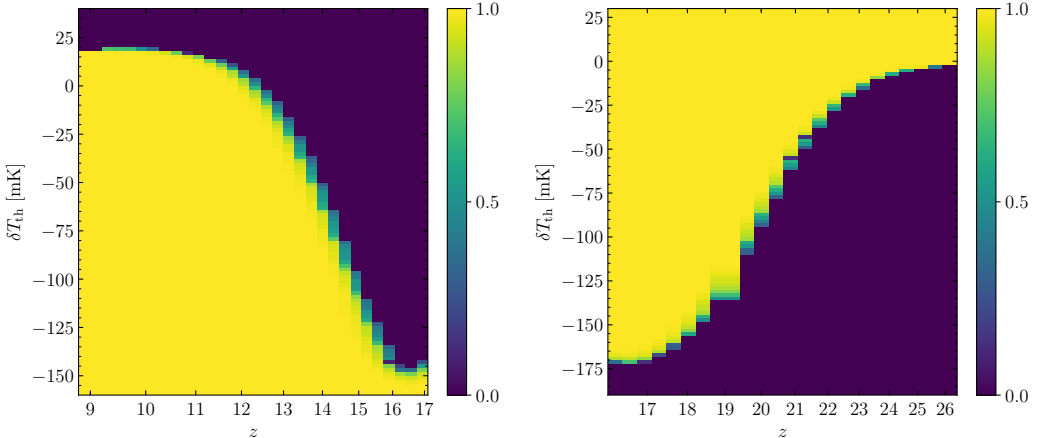


Figure 5.14. Order parameters of the 21 cm brightness field during heating (left) and cooling (right) as a function of redshift and threshold. Cells are considered filled during heating if they are *above* δT_{th} , and during cooling if they are *below* δT_{th} .

On the other hand, during cooling we use a reversed thresholding and consider a cell cold if it has $\delta T_b \leq \delta T_{\text{th}}$. For this process, we track the OP over redshifts $z \sim 16\text{--}26$. In both cases, we smooth the signal over two cells and sample it at logarithmically spaced intervals.

The results are shown in Figure 5.14, where the thresholds are sampled every 2 mK. The order parameter varies significantly depending on the threshold chosen. Below $\delta T_{\text{th}} \approx -150$ mK, there are no further dynamics in the percolation of hot regions. Cold spots percolate at temperatures as low as 170 mK during the coldest periods of the signal. The order parameter of the mean-subtracted field was also calculated, but a meaningful interpretation of such a percolation process, where the threshold varies significantly through time, is difficult to propose. However, the shifts in the OP generally follow the mean temperature and deviations occur during the bulk of the transitions, when the average temperature changes most rapidly.

An interesting result comes from scaling the redshift dependency to filling fractions at any given threshold. Figure 5.15 shows line plots extracted from Figure 5.14 at thresholds $\delta T_{\text{th}} = 4$ mK, -10 mK, -30 mK, -70 mK and -130 mK. On the left, the OP is plotted as a function of redshift and the threshold clearly determines the evolution of percolation. On the right, the OP is shown as a function of the filling fraction of hot spots, x_{hot} , i.e. the fractional volume of gas above any given threshold temperature. This fraction absorbs the dependency on threshold and we see a collapse of the order parameter onto a single curve.

The critical fraction of hot spots is found to be (on average) $x_{\text{hot},c} \approx 0.07$, with a scatter of 0.01 over all threshold from -140 mK to 14 mK. The sampling in filling fraction is quite coarse at the current redshift resolution. However, the critical fraction can still be constrained to values less than $x_{\text{hot}} \sim 0.1$.

Figure 5.16 shows the same calculation for the cooling transition, where

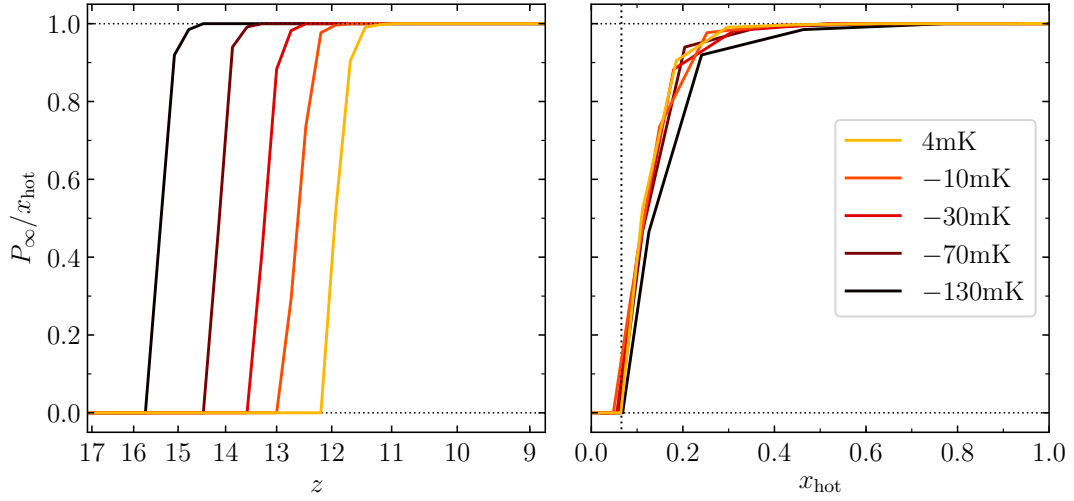


Figure 5.15. Order parameter during heating for various threshold temperatures, as a function of redshift (left) and filling fraction (right).

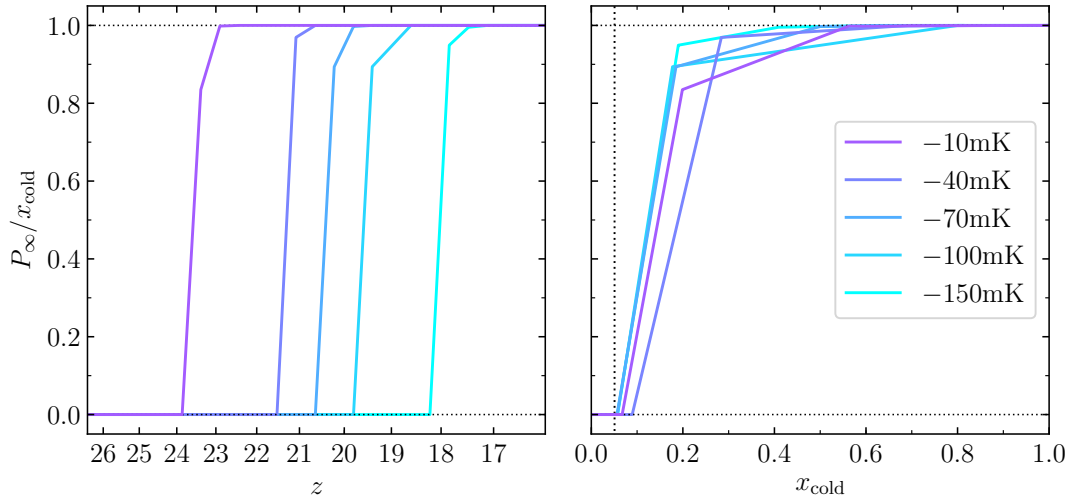


Figure 5.16. Same as Figure 5.15 but for the cooling phase and at different thresholds.

x_{cold} is the fractional volume of gas below a given threshold. The critical fraction of cold spots is found to be $x_{\text{cold},c} \approx 0.05$, with a scatter of 0.02 over the threshold range -160 mK to -10 mK , yet the sampling is even coarser in this case. Therefore, this value is a fairly vague lower limit, with an upper bound at $x_{\text{cold}} \sim 0.2$. The correlations during cooling should not be any different to heating, since both processes are driven by heat diffusion, so a mirrored order parameter could be expected when properly resolved. Any deviation from this would be a clear indication of the properties of the underlying density field. Note that once again we have the formation of a percolating cluster at critical filling fractions much lower than that of a random process, even with these loose bounds.

5.2.2 Minkowski functionals

Much of the same discussion for the Minkowski functionals during reionization applies to heating and cooling. The results are shown in Figures 5.17 to 5.26 with the same presentation scheme used for reionization, and here we discuss the notable differences to reionization.

During heating, $V_0 = 0.07$ can be seen to match the average position of the critical fraction; while the same applies at $V_0 = 0.95$ during cooling. This corresponds to a filling fraction for cold spots of 0.05. We keep the same thresholding direction for both phases, such that they are direct continuations of each other. Again, these are not very accurate calculations.

During cooling, the peak in surface area shifts to lower temperatures and broadens, while also becoming more pronounced. This is consistent with cold spots of the same temperature clustering to form filamentary shapes. During the bulk of the transition, the front end of the curve extends further than the tail, as the coldest spots cluster more rapidly. Notice how the reverse occurs during heating with an even more asymmetric curve. This would agree with heating occurring everywhere at vastly different paces.

The extrema of V_2 once again lie at the critical points for both processes. For heating this is the maximum, since we define hot spots to belong in the excursion set on which we calculate the MFs. The opposite occurs with cold spots, since we define them in the complement of this set. In both cases we see that the relevant points provide consistent upper bounds on the critical fraction, as we had found previously. Notice also that the curves for V_2 broaden at the redshifts centered in the bulk transitions for the same reasons as the surface area.

The zeros of the Euler characteristic match the extrema of V_2 as for reionization. Its own extrema are heightened at the end of cooling and the start of reionization. In particular, the amplified minimum shows the existence of structures containing many tunnels. This would agree with strongly clustered cold spots forming a single percolating cluster which intertwines with a percolating cluster of hot gas—an overlap phase for heating and cooling. The same feature is seen during the reionization overlap phase, which we now show in the full 21 cm brightness temperature, as spin temperature fluctuations sourced by the gas kinetic temperature cede their role to the ionization field.

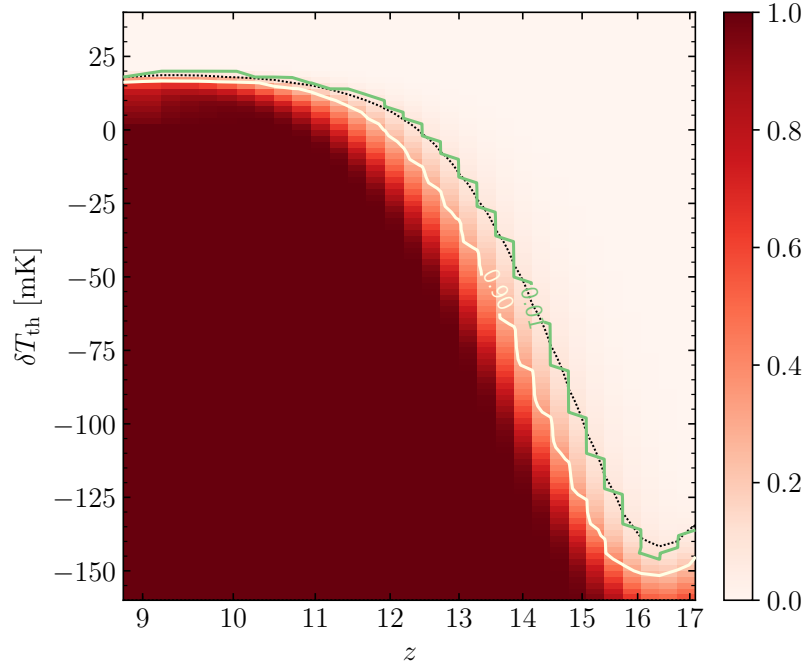


Figure 5.17. V_0 during heating. The contour $V_0 = 0.07$ is shown in dotted black. The contours $P_\infty/x_{\text{hot}} = 0.01$ and 0.90 are shown in green and white, respectively.

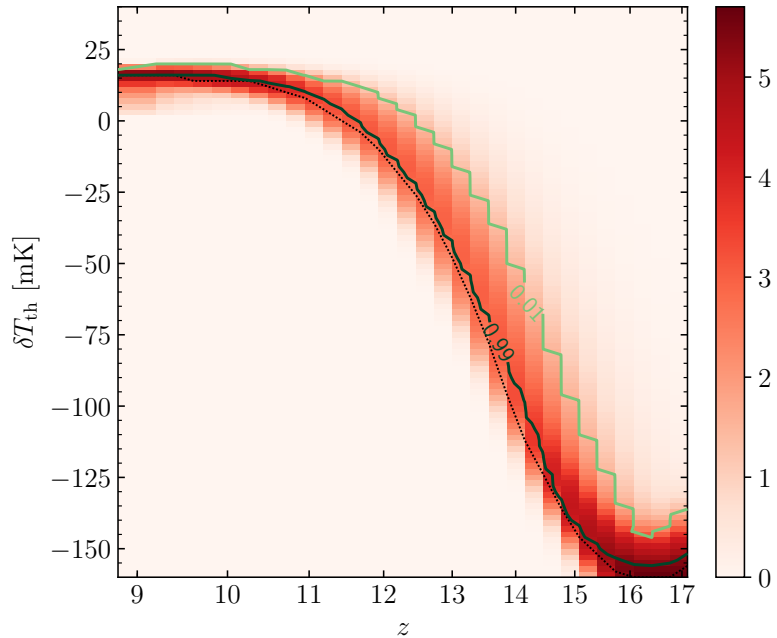


Figure 5.18. V_1 for the same. The dotted black line represents the maximum of $V_1(\delta T_{\text{th}}; z)$. $P_\infty/x_{\text{hot}} = 0.90$ is shown in solid black.

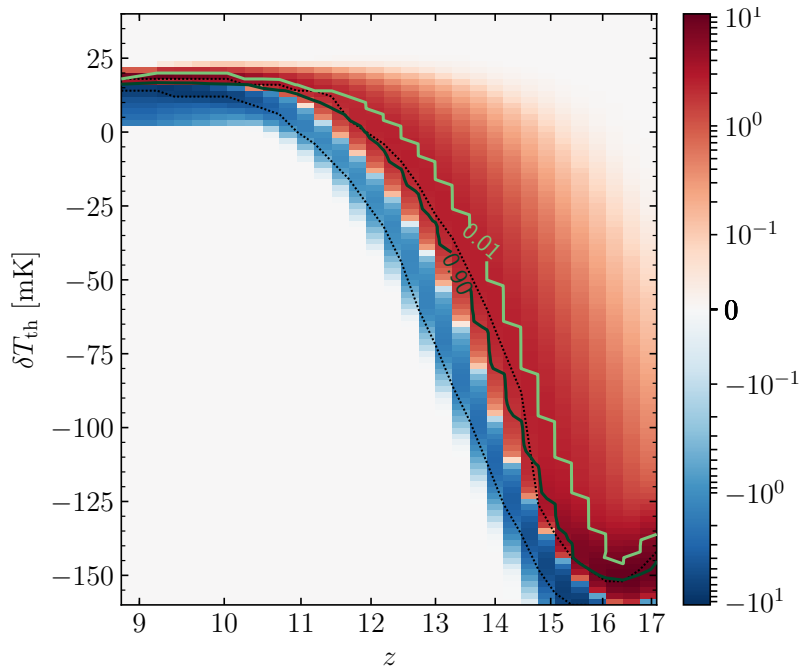


Figure 5.19. $V_2 \cdot 10^{-1}$ during heating. The maximum and minimum of $V_2(\delta T_{\text{th}}; z)$ are highlighted by the dotted black lines. Note the colormap is logarithmically scaled to make visible the tails of the curves.

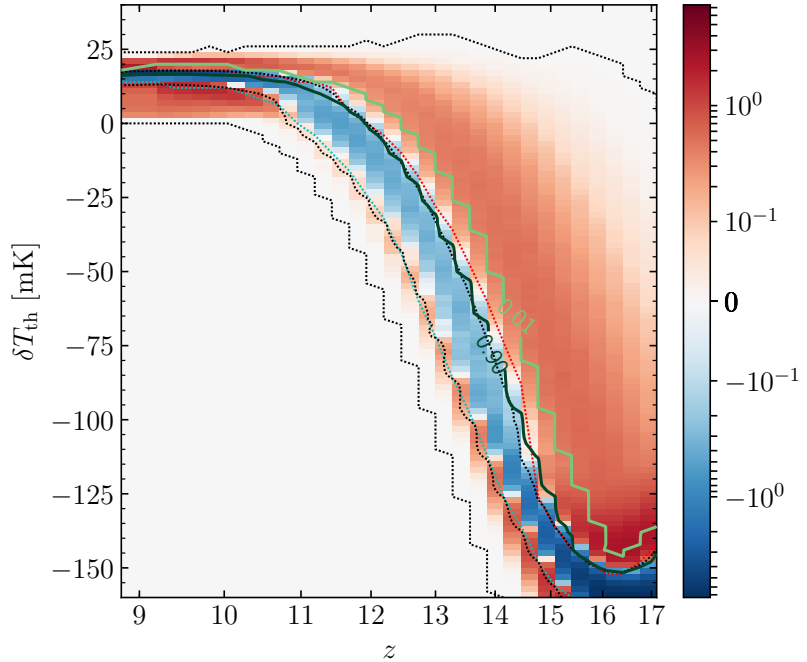


Figure 5.20. $V_3 \cdot 10^{-3}$ for the same. The maximum and minimum of $V_2(\delta T_{\text{th}}; z)$ are shown in dotted red and cyan, respectively. The dotted black lines represent the zeros of $V_3(\delta T_{\text{th}}; z)$.

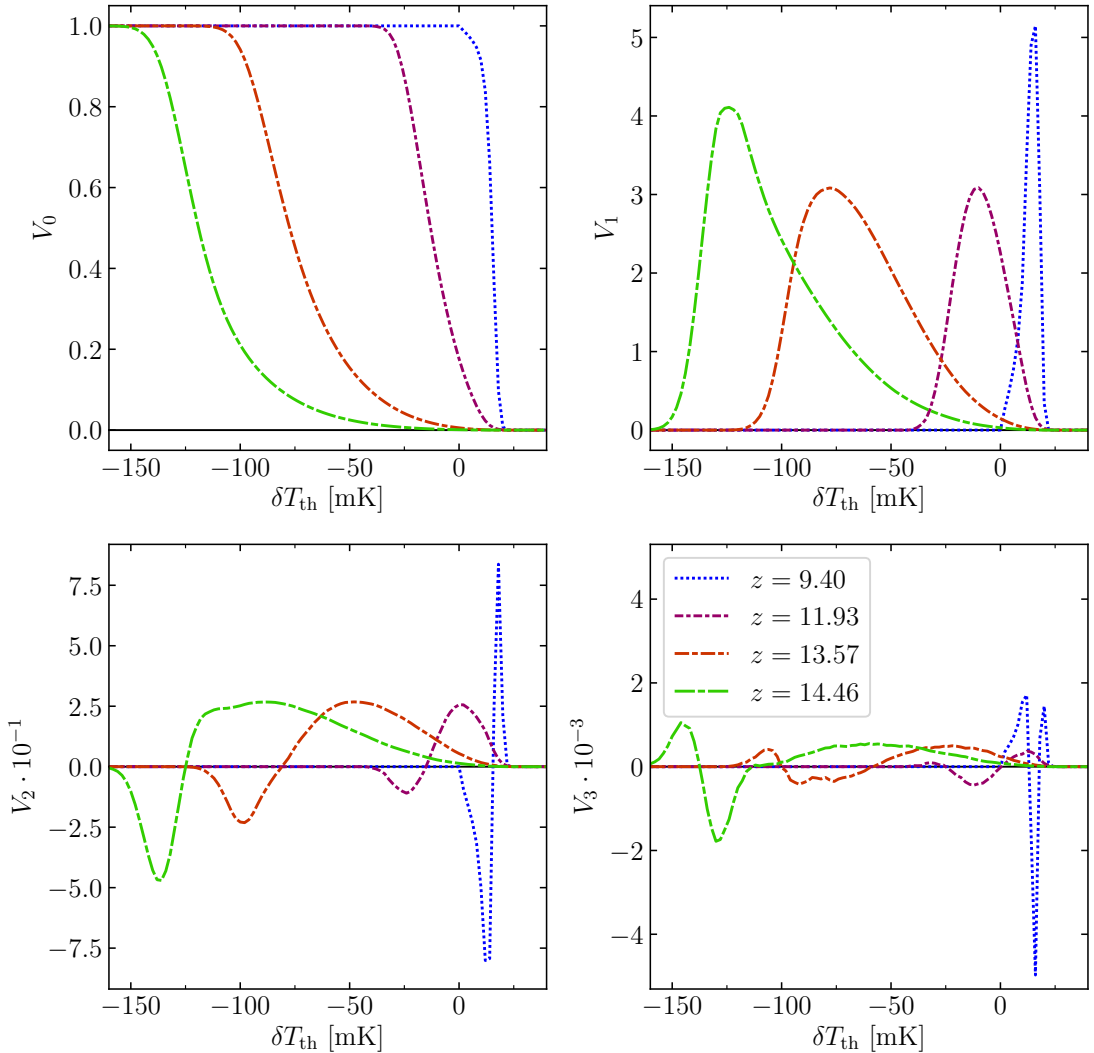


Figure 5.21. Line plots of the MFs during heating, shown at redshifts $z = 9.40$ (blue), 11.93 (purple), 13.57 (red) and 14.46 (green).

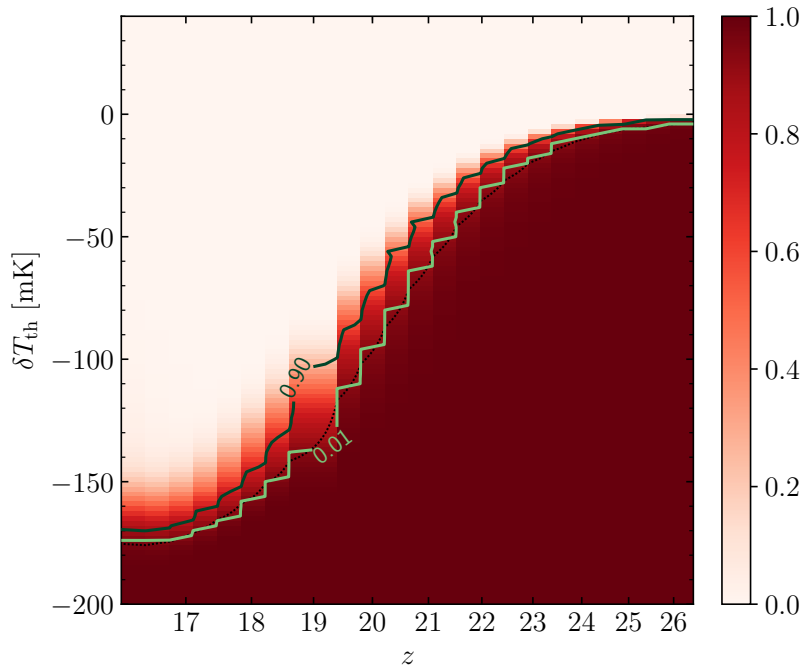


Figure 5.22. V_0 during cooling. The contour $V_0 = 0.95$ is shown in dotted black.

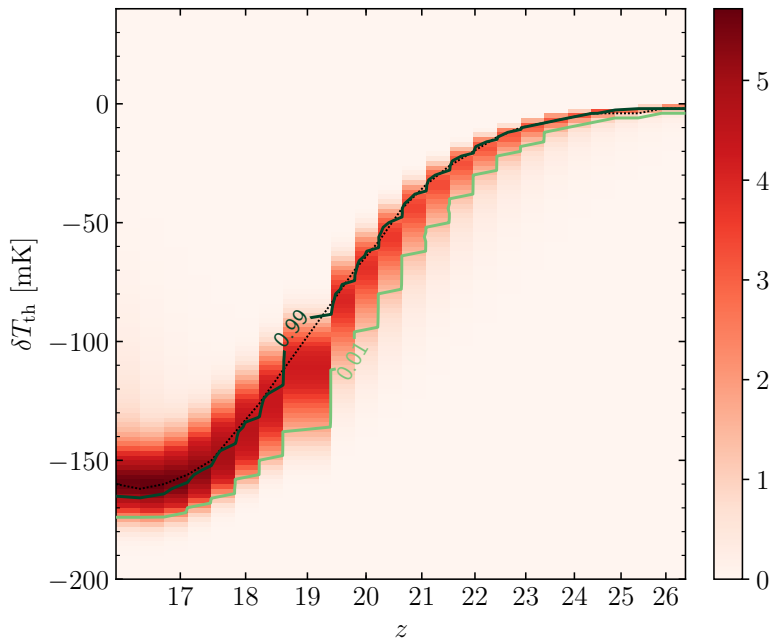


Figure 5.23. V_1 for the same. The dotted black line represents the maximum.

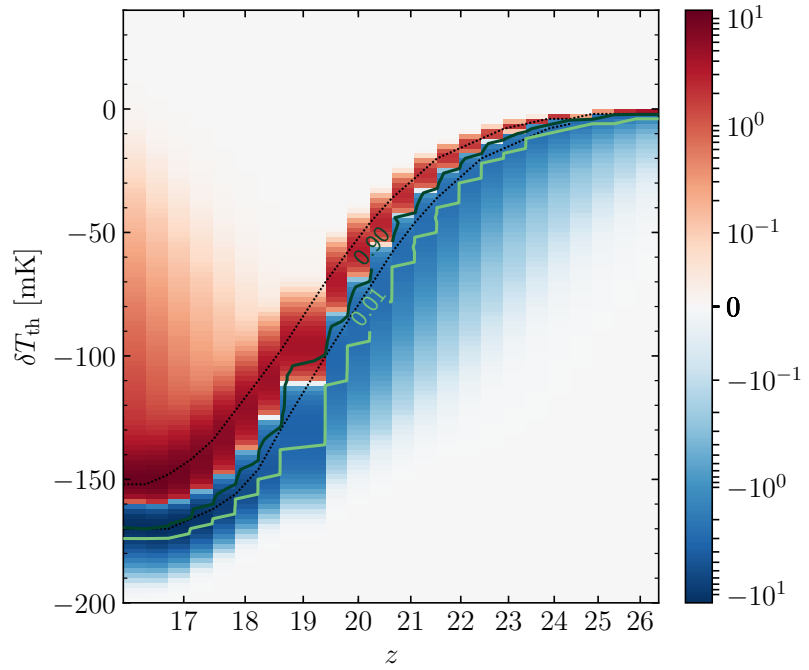


Figure 5.24. $V_2 \cdot 10^{-1}$ during cooling. The dotted black lines represent extrema.

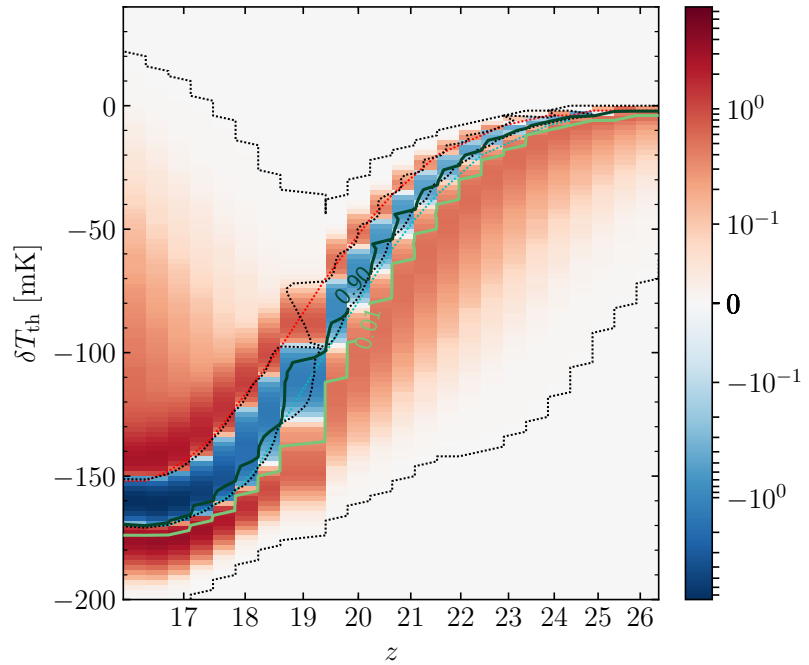


Figure 5.25. $V_3 \cdot 10^{-3}$ for the same. The extrema of $V_2(\delta T_{\text{th}}; z)$ are shown in dotted red and cyan, corresponding to the maximum and minimum, respectively. The dotted black lines represent zero contours of V_3 .

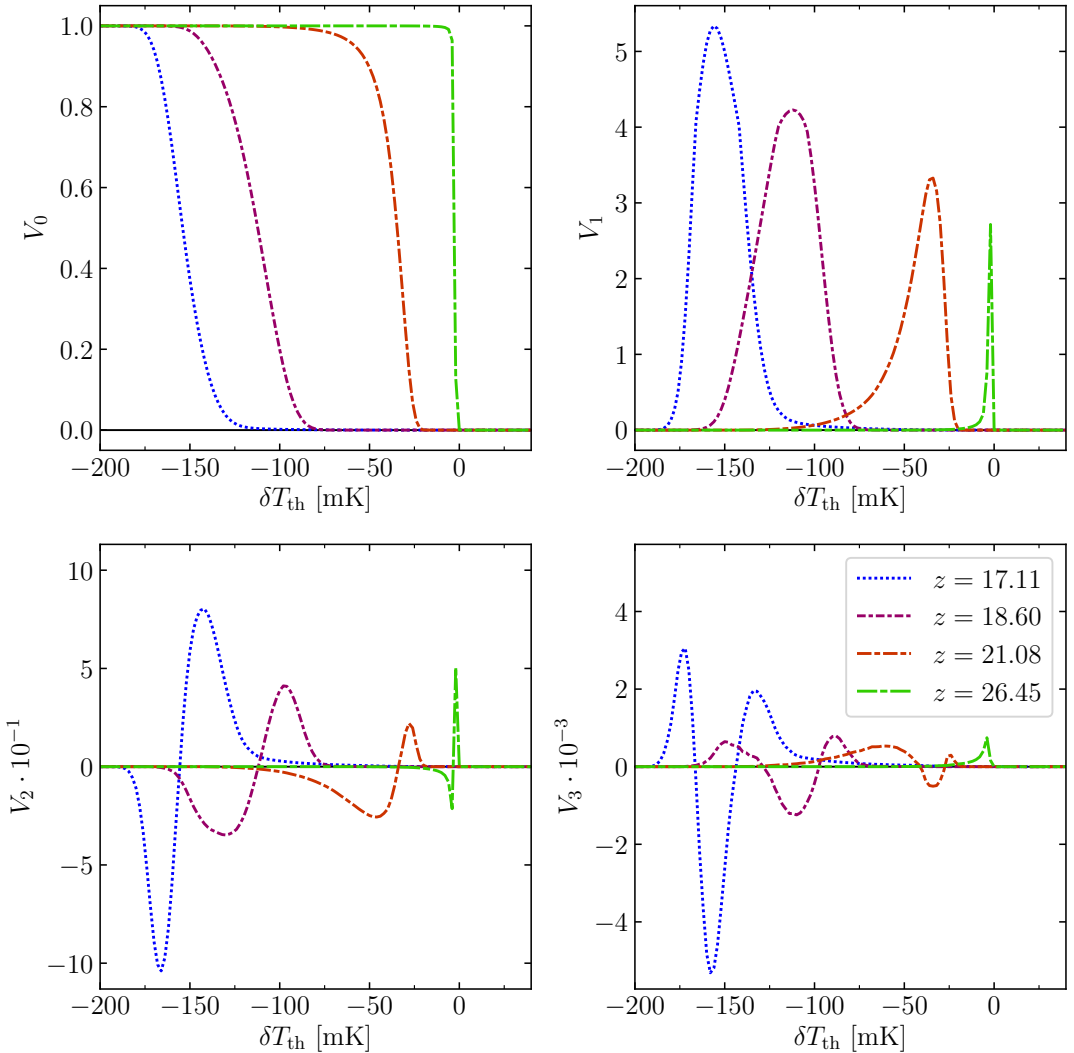


Figure 5.26. Line plots of the MFs during cooling, shown at redshifts $z = 17.11$ (blue), 18.60 (purple), 21.08 (red) and 26.45 (green).

CHAPTER 6

Conclusion

Mapping the first billion years of the Universe is made possible with the 21 cm signal. Using a simulated signal from high redshifts, this project has studied reionization and the preceding cosmic phases of heating and cooling as formal percolation processes. We state these in terms of a well-defined order parameter from the theory for random fields. Our understanding of these processes was arrived at by first studying Gaussian random fields and the role of correlations in measures of order and geometry.

We have found that percolating clusters form within the H II and H I distributions at very low filling fractions in the respective media. These quickly absorb all other clusters, organizing into a complex topology that allows them to intertwine and coexist during an overlap period which extends throughout most of reionization. The heating and cooling transitions form percolating clusters at similarly low filling fractions and have an analogous overlap phase around the turnover point in the mean 21 cm brightness temperature.

The size characteristics of the ionization field were found to agree with the scale-free behaviour of critical phenomena. Through granulometry we observe a percolating cluster which exhibits a filamentary structure dominated by small-scale features for the duration of reionization.

Minkowski functionals were found to be closely linked to the evolution of the order parameter. Specifically, the extrema in integral mean curvature and the zeros in integral Gaussian curvature were found to place robust upper bounds on the critical filling fraction of the percolation processes discussed. Reionization, heating and cooling present percolation models with different physics underlying correlations between states. Therefore, the connections between Minkowski functionals and the order parameter might be more universal aspects of random fields and percolation.

Our results follow from a specific set of simulations. In future work, a precise investigation into their dependency on physical parameters and reionization models would clarify the extent of their validity. There are also many other avenues to be explored in the study of correlations in the high redshift Universe. Criticality appears to be a promising perspective and measures

other than the order parameter, such as connectivity and centrality, are yet to be tested. We hope the powerful tools from various areas of physics and mathematics will continue to be used in synergy when analyzing future 21 cm observations.

References

- Abrahamsen, P. (1997). *A review of gaussian random fields and correlation functions* (2nd ed.). Oslo, Norway: Norwegian Computing Center. Retrieved from http://publications.nr.no/2437/Abrahamsen_-_A_Review_of_Gaussian_random_fields_and_correlation.pdf
- Adler, R. J., & Taylor, J. E. (2007). *Random fields and geometry*. New York, NY: Springer. DOI: [10.1007/978-0-387-48116-6](https://doi.org/10.1007/978-0-387-48116-6)
- ALMA. (n.d.). *Homepage*. Retrieved 14/04/2018, from <http://www.almaobservatory.org/en/home/>
- Ballesteros, H. G., Fernández, L. A., Martín-Mayor, V., Muñoz Sudupe, A., Parisi, G., & Ruiz-Lorenzo, J. J. (1999). Scaling corrections: site percolation and ising model in three dimensions. *Journal of Physics A: Mathematical and General*, 32(1), 1–13. DOI: [10.1088/0305-4470/32/1/004](https://doi.org/10.1088/0305-4470/32/1/004)
- Blackman, E. G. (n.d.). *Physics of astrophysics i: Radiative processes*. Lecture notes. University of Rochester. Retrieved 20/04/2018, from <http://www.pas.rochester.edu/~blackman/ast461/lectures.pdf>
- Bowman, J. D., Rogers, A. E. E., Monsalve, R. A., Mozdzen, T. J., & Mahesh, N. (2018). An absorption profile centred at 78 megahertz in the sky-averaged spectrum. *Nature*, 555, 67–70. DOI: [10.1038/nature25792](https://doi.org/10.1038/nature25792)
- Bradley, R. F. (2017). The precision array for probing the epoch of reionization (paper): A modern scientific adventure. *URSI Radio Science Bulletin*, 2017(362), 39-52. DOI: [10.23919/URSIRSB.2017.8267372](https://doi.org/10.23919/URSIRSB.2017.8267372)
- Christensen, K., & Moloney, N. R. (2005). *Complexity and criticality*. London, England: Imperial College Press. Retrieved from <https://www.worldscientific.com/worldscibooks/10.1142/p365#t=aboutBook>
- DeBoer, D. R., Parsons, A. R., Aguirre, J. E., Alexander, P., Ali, Z. S., Beardsley, A. P., ... Zheng, H. (2017). Hydrogen epoch of reionization array (HERA). *Publications of the Astronomical Society of the Pacific*, 129(974), 045001. DOI: [10.1088/1538-3873/129/974/045001](https://doi.org/10.1088/1538-3873/129/974/045001)
- Eriksen, H. K., Novikov, D. I., Lilje, P. B., Banday, A. J., & Górski, K. M. (2004). Testing for non-gaussianity in the wilkinson microwave anisotropy probe data: Minkowski functionals and the length of the skeleton. *The Astrophysical Journal*, 612(1), 64–80. DOI: [10.1086/422570](https://doi.org/10.1086/422570)

- Field, G. B. (1958). Excitation of the hydrogen 21-cm line. *Proceedings of the IRE*, 46(1), 240–250. DOI: [10.1109/JRPROC.1958.286741](https://doi.org/10.1109/JRPROC.1958.286741)
- Friedrich, M. M., Mellema, G., Alvarez, M. A., Shapiro, P. R., & Iliev, I. T. (2011). Topology and sizes of h ii regions during cosmic reionization. *Monthly Notices of the Royal Astronomical Society*, 413(2), 1353–1372. DOI: [10.1111/j.1365-2966.2011.18219.x](https://doi.org/10.1111/j.1365-2966.2011.18219.x)
- Furlanetto, S. R. (2016). The 21-cm line as a probe of reionization. In *Understanding the epoch of cosmic reionization* (Vol. 423). Switzerland: Springer International Publishing. DOI: [10.1007/978-3-319-21957-8](https://doi.org/10.1007/978-3-319-21957-8)
- Furlanetto, S. R., & Oh, S. P. (2016). Reionization through the lens of percolation theory. *Monthly Notices of the Royal Astronomical Society*, 457(2), 1813–1827. DOI: [10.1093/mnras/stw104](https://doi.org/10.1093/mnras/stw104)
- Furlanetto, S. R., Oh, S. P., & Briggs, F. H. (2006). Cosmology at low frequencies: The 21cm transition and the high-redshift universe. *Physics Reports*, 433(4), 181–301. DOI: <https://doi.org/10.1016/j.physrep.2006.08.002>
- Furlanetto, S. R., Zaldarriaga, M., & Hernquist, L. (2004). The growth of h ii regions during reionization. *The Astrophysical Journal*, 613(1), 1–15. DOI: [10.1086/423025](https://doi.org/10.1086/423025)
- Giri, S. K., Mellema, G., Dixon, K. L., & Iliev, I. T. (2018). Bubble size statistics during reionization from 21-cm tomography. *Monthly Notices of the Royal Astronomical Society*, 473(3), 2949–2964. DOI: [10.1093/mnras/stx2539](https://doi.org/10.1093/mnras/stx2539)
- Gleser, L., Nusser, A., Ciardi, B., & Desjacques, V. (2006). The morphology of cosmological reionization by means of minkowski functionals. *Monthly Notices of the Royal Astronomical Society*, 370(3), 1329–1338. DOI: [10.1111/j.1365-2966.2006.10556.x](https://doi.org/10.1111/j.1365-2966.2006.10556.x)
- GMTO (Ed.). (2012). *Giant magellan telescope, scientific promise and opportunities*. Retrieved 14/04/2018, from https://www.gmto.org/Resources/GMT-SCI-REF-00482_2_GMT_Science_Book.pdf
- Gonzalez, R. C., & Woods, R. E. (2008). *Digital image processing* (3rd ed.). Upper Saddle River, NJ: Pearson Prentice Hall. Retrieved from <https://www.pearson.com/us/higher-education/product/Gonzalez-Digital-Image-Processing-3rd-Edition-9780131687288.html>
- Gunn, J. E., & Peterson, B. A. (1965). On the density of neutral hydrogen in intergalactic space. *Astrophysical Journal*, 142, 1633–1641. DOI: [10.1086/148444](https://doi.org/10.1086/148444)
- Hadwiger, H. (1957). *Vorlesungen über inhalt, oberfläche und isoperimetrie*. Berlin, Germany: Springer-Verlag. DOI: [10.1007/978-3-642-94702-5](https://doi.org/10.1007/978-3-642-94702-5)
- Holmes-Cerfon, M. (2008). *Generating stationary gaussian random fields*. Retrieved 23/04/2018, from https://cims.nyu.edu/~holmes/mathcamp/ft_summary.pdf

- Hoshen, J., & Kopelman, R. (1976). Percolation and cluster distribution. *Phys. Rev. B*, *14*, 3438–3445. DOI: [10.1103/PhysRevB.14.3438](https://doi.org/10.1103/PhysRevB.14.3438)
- Kakiichi, K., Majumdar, S., Mellema, G., Ciardi, B., Dixon, K. L., Iliev, I. T., ... Busch, P. (2017). Recovering the H II region size statistics from 21-cm tomography. *Monthly Notices of the Royal Astronomical Society*, *471*(2), 1936–1954. DOI: [10.1093/mnras/stx1568](https://doi.org/10.1093/mnras/stx1568)
- Lee, K.-G., Cen, R., Gott III, J. R., & Trac, H. (2008). The topology of cosmological reionization. *The Astrophysical Journal*, *675*(1), 8–15. DOI: [10.1086/525520](https://doi.org/10.1086/525520)
- Lin, Y., Oh, S. P., Furlanetto, S. R., & Sutter, P. M. (2016). The distribution of bubble sizes during reionization. *Monthly Notices of the Royal Astronomical Society*, *461*(3), 3361–3374. DOI: [10.1093/mnras/stw1542](https://doi.org/10.1093/mnras/stw1542)
- Loeb, A., & Furlanetto, S. R. (2013). *The first galaxies in the universe*. Princeton, NJ: Princeton University Press. Retrieved from <https://press.princeton.edu/titles/9914.html>
- LOFAR. (n.d.). *Homepage*. Retrieved 14/04/2018, from <http://www.lofar.org/>
- Lorenz, C. D., & Ziff, R. M. (1998). Universality of the excess number of clusters and the crossing probability function in three-dimensional percolation. *Journal of Physics A: Mathematical and General*, *31*(40), 8147–8157. DOI: [10.1088/0305-4470/31/40/009](https://doi.org/10.1088/0305-4470/31/40/009)
- Mecke, K. R. (2000). Additivity, convexity, and beyond: Applications of minkowski functionals in statistical physics. In K. R. Mecke & D. Stoyan (Eds.), *Statistical physics and spatial statistics* (pp. 111–184). Berlin, Heidelberg: Springer Berlin Heidelberg. DOI: [10.1007/3-540-45043-2_6](https://doi.org/10.1007/3-540-45043-2_6)
- Mecke, K. R., & Wagner, H. (1991). Euler characteristic and related measures for random geometric sets. *Journal of Statistical Physics*, *64*(3), 843–850. DOI: [10.1007/BF01048319](https://doi.org/10.1007/BF01048319)
- Mellema, G., Koopmans, L. V. E., Abdalla, F. A., Bernardi, G., Ciardi, B., Daiboo, S., ... Zaroubi, S. (2013, 01). Reionization and the cosmic dawn with the square kilometre array. *Experimental Astronomy*, *36*(1), 235–318. DOI: [10.1007/s10686-013-9334-5](https://doi.org/10.1007/s10686-013-9334-5)
- Mesinger, A., Furlanetto, S., & Cen, R. (2011). 21cmfast: a fast, seminumerical simulation of the high-redshift 21-cm signal. *Monthly Notices of the Royal Astronomical Society*, *411*(2), 955–972. DOI: [10.1111/j.1365-2966.2010.17731.x](https://doi.org/10.1111/j.1365-2966.2010.17731.x)
- Mo, H., van den Bosch, F., & White, S. (2010). *Galaxy formation and evolution*. New York, NY: Cambridge University Press. Retrieved from <http://www.cambridge.org/gb/academic/subjects/physics/astrophysics/galaxy-formation-and-evolution-1?format=HB&isbn=9780521857932>
- NCRA. (n.d.). *GMRT homepage*. Retrieved 14/04/2018, from <http://www.ncra.tifr.res.in/ncra/gmrt>

- Newman, C. M., & Schulman, L. S. (1981). Infinite clusters in percolation models. *Journal of Statistical Physics*, 26(3), 613–628. DOI: [10.1007/BF01011437](https://doi.org/10.1007/BF01011437)
- Newman, M. E. J., & Ziff, R. M. (2000). Efficient monte carlo algorithm and high-precision results for percolation. *Phys. Rev. Lett.*, 85, 4104–4107. DOI: [10.1103/PhysRevLett.85.4104](https://doi.org/10.1103/PhysRevLett.85.4104)
- Oesch, P. A., Brammer, G., van Dokkum, P. G., Illingworth, G. D., Bouwens, R. J., Labb  , I., ... Willner, S. P. (2016). A remarkably luminous galaxy at $z = 11.1$ measured with hubble space telescope grism spectroscopy. *The Astrophysical Journal*, 819(2), 129. DOI: [10.3847/0004-637X/819/2/129](https://doi.org/10.3847/0004-637X/819/2/129)
- Pritchard, J. R., & Loeb, A. (2012). 21 cm cosmology in the 21st century. *Reports on Progress in Physics*, 75(8), 086901. DOI: [10.1088/0034-4885/75/8/086901](https://doi.org/10.1088/0034-4885/75/8/086901)
- Rybicki, G. (1979). *Radiative processes in astrophysics*. New York, NY: Wiley. Retrieved from <https://www.wiley.com/en-gb/Radiative+Processes+in+Astrophysics-p-9780471827597>
- Schmalzing, J., & Buchert, T. (1997). Beyond genus statistics: A unifying approach to the morphology of cosmic structure. *The Astrophysical Journal Letters*, 482(1), L1–L4. DOI: [10.1086/310680](https://doi.org/10.1086/310680)
- Schmalzing, J., & G  rski, K. M. (1998). Minkowski functionals used in the morphological analysis of cosmic microwave background anisotropy maps. *Monthly Notices of the Royal Astronomical Society*, 297(2), 355–365. DOI: [10.1046/j.1365-8711.1998.01467.x](https://doi.org/10.1046/j.1365-8711.1998.01467.x)
- SKA Org. (Ed.). (2015). *Advancing astrophysics with the square kilometre array*. Dolman Scott. Retrieved from <https://www.skatelescope.org/books/>
- STScI. (2012). *James webb space telescope, science guide*. Retrieved 14/04/2018, from https://www.nasa.gov/pdf/715962main_jwst_science_pub-v1-2.pdf
- Yaglom, A. M. (1987). *Correlation theory of stationary and related random functions* (Vol. 1). New York, NY: Springer-Verlag. Retrieved from <https://www.springer.com/gb/book/9781461290865>
- Yoshiura, S., Shimabukuro, H., Takahashi, K., & Matsubara, T. (2017). Studying topological structure of 21-cm line fluctuations with 3d minkowski functionals before reionization. *Monthly Notices of the Royal Astronomical Society*, 465(1), 394–402. DOI: [10.1093/mnras/stw2701](https://doi.org/10.1093/mnras/stw2701)
- Zahn, O., Lidz, A., McQuinn, M., Dutta, S., Hernquist, L., Zaldarriaga, M., & Furlanetto, S. R. (2007). Simulations and analytic calculations of bubble growth during hydrogen reionization. *The Astrophysical Journal*, 654(1), 12–26. DOI: [10.1086/509597](https://doi.org/10.1086/509597)
- Zaroubi, S. (2013). The epoch of reionization. In T. Wiklind, B. Mabasher, & V. Bromm (Eds.), *The first galaxies: Theoretical predictions and observational clues* (pp. 45–101). Berlin, Heidelberg: Springer Berlin Hei-

delberg. DOI: [10.1007/978-3-642-32362-1_2](https://doi.org/10.1007/978-3-642-32362-1_2)

Zitrin, A., Labb  , I., Belli, S., Bouwens, R., Ellis, R. S., Roberts-Borsani, G., ...

Smit, R. (2015). Ly α emission from a luminous $z = 8.68$ galaxy: Implications for galaxies as tracers of cosmic reionization. *The Astrophysical Journal Letters*, 810(1), L12. DOI: [10.1088/2041-8205/810/1/L12](https://doi.org/10.1088/2041-8205/810/1/L12)